RESEARCH ARTICLE

Key Points:
- Altimeters can resolve the seasonal circulation over the SW Atlantic coastal shelf
- Seasonal changes are primarily wind-driven north of the Rio de la Plata
- Our results agree with previous studies using models and field surveys

Supporting Information:
- Supporting Information S1

Correspondence to:
P. T. Strub,
tstrub@coas.oregonstate.edu

Altimeter-derived seasonal circulation on the southwest Atlantic shelf: 27°–43°S

P. Ted Strub[1], Corinne James[1], Vincent Combes[1], Ricardo P. Matano[1], Alberto R. Piola[2], Elbio D. Palma[3], Martin Saraceno[4], Raul A. Guerrero[5], Harold Fenco[5], and Laura A. Ruiz-Etcheverry[4]

[1]College of Earth, Ocean, and Atmospheric Sciences, Oregon State University, Corvallis, Oregon, USA, [2]Departamento Oceanografía, Servicio de Hidrografía Naval and Departamento de Ciencias de la Atmósfera y los Océanos, Universidad de Buenos Aires, and UMI/IFAECI, CONICET-CNRS-UBA, Buenos Aires, Argentina, [3]Departamento de Física, Universidad Nacional del Sur and Instituto Argentino de Oceanografía, Bahía Blanca, Argentina, [4]Centro de Investigaciones del Mar y la Atmósfera, CONICET, Departamento de Ciencias de la Atmósfera y los Océanos, Universidad de Buenos Aires, and UMI/IFAECI, CONICET-CNRS-UBA, Buenos Aires, Argentina, [5]Instituto Nacional de Investigación y Desarrollo Pesquero, Mar del Plata, Argentina

Abstract Altimeter sea surface height (SSH) fields are analyzed to define and discuss the seasonal circulation over the wide continental shelf in the SW Atlantic Ocean (27°–43°S) during 2001–2012. Seasonal variability is low south of the Rio de la Plata (RdlP), where winds and currents remain equatorward for most of the year. Winds and currents in the central and northern parts of our domain are also equatorward during autumn and winter but reverse to become poleward during spring and summer. Transports of shelf water to the deep ocean are strongest during summer offshore and to the southeast of the RdlP. Details of the flow are discussed using mean monthly seasonal cycles of winds, heights, and currents, along with analyses of Empirical Orthogonal Functions. Principle Estimator Patterns bring out the patterns of wind forcing and ocean response. The largest part of the seasonal variability in SSH signals is due to changes in the wind forcing (described above) and changes in the strong boundary currents that flow along the eastern boundary of the shelf. The rest of the variability contains a smaller component due to heating and expansion of the water column, concentrated in the southern part of the region next to the coast. Our results compare well to previous studies using in situ data and to results from realistic numerical models of the regional circulation.

1. Introduction and Background

In this paper, we use altimeter sea surface height (SSH) and associated geostrophic currents to investigate the seasonal variability of the surface circulation over and next to the wide continental shelf in the SW Atlantic off northern Argentina, Uruguay, and southern Brazil. The specific region of interest over the shelf between approximately 27°–43°S is located inshore of the larger-scale energetic western boundary current region depicted in Figure 1 and described in the next section. The systematically collected 2-D altimeter fields confirm and integrate the conceptual picture of the regional shelf circulation that has been pieced together from more sporadic and sparse field data and recent numerical models. These previous results are reviewed briefly in the next section and compared to the altimeter results in the Discussion section 4.2.

1.1. Background: Previous Investigations of the Shelf and Deep Ocean Circulation in the SW Atlantic

The deep ocean circulation of the SW Atlantic is characterized by the poleward flow of the warm and salty Brazil Current (BC) in the north and the equatorward flow of the cold and relatively fresh Malvinas Current (MC) in the south (Figure 1). The two western boundary currents meet near 38°S, generating the highly energetic Brazil/Malvinas Confluence (BMC), which is characterized by the continuous formation of warm and cold core eddies and filaments [*Gordon and Greengrove*, 1986; *Gordon*, 1989]. The continental shelf in this region is a relatively shallow plateau (< 200 m) of variable width narrowing northward from about 400 km at 40°S to ∼ 95 km at 31°S. The region is characterized by seasonally varying winds and moderate tides [e.g., *Palma et al.*, 2004a, 2004b]. The hydrographic structure is represented by two water masses: south of 35°S the shelf is mostly occupied by the relatively cold and fresh (∼ 33.7) Subantarctic Shelf Water [SASW, *Piola et al.*, 2000; *Lucas et al.*, 2005]. North of about 34°S, the shelf is filled by mixtures of warm, salty
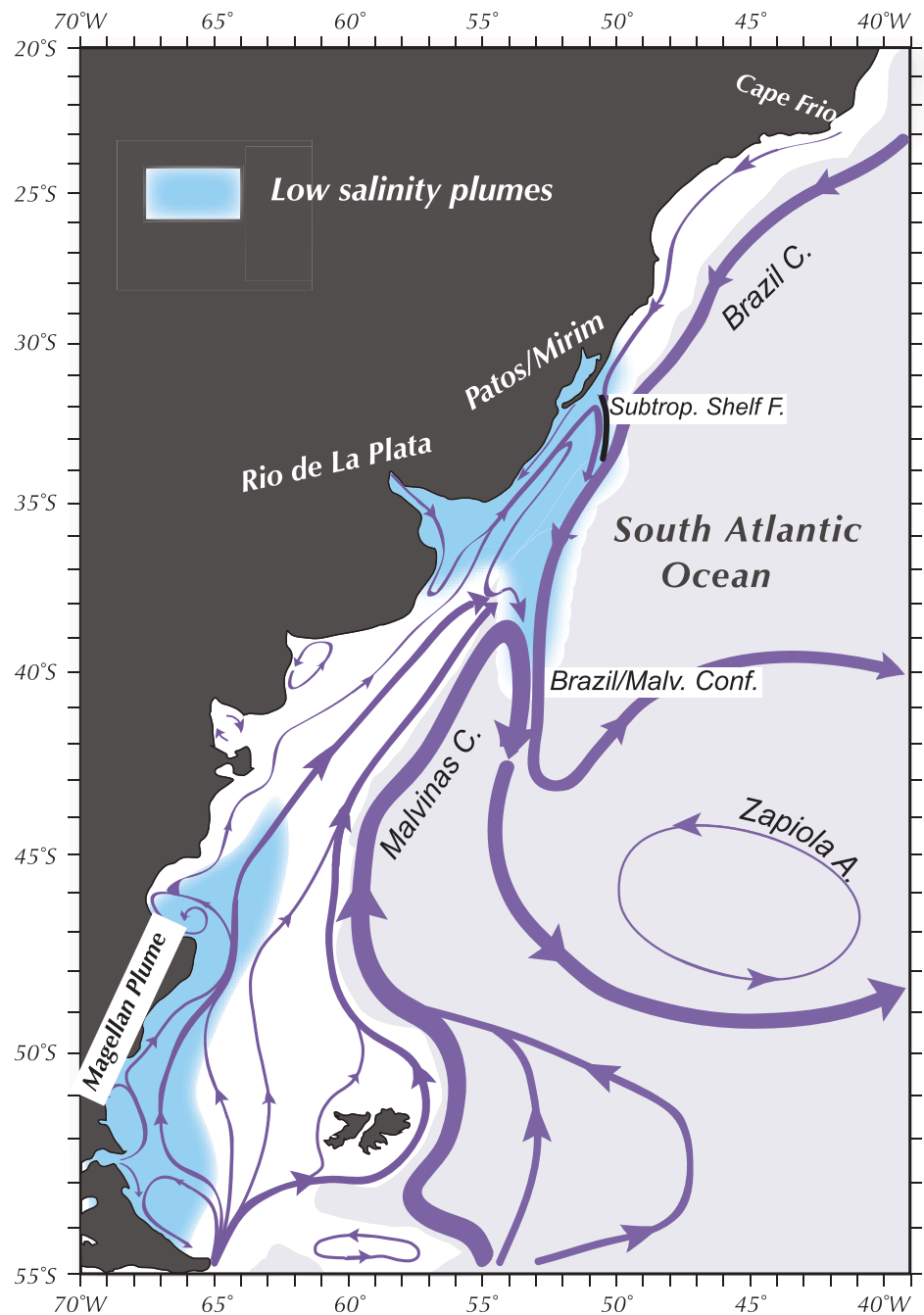
Figure 1. Schematic depiction of the circulation in the SW Atlantic Ocean. The blue color emanating from the Rio de la Plata and the Strait of Magellan denotes SSS < 33.5. The black line represents the STSF.

(> 35) subtropical waters derived from the BC, with low salinity waters added from the Rio de la Plata (RdlP), Patos-Mirim Lagoon (PML), and other local sources of continental runoff. This water mass is referred to as Subtropical Shelf Water [STSW, *Piola et al.*, 2000; *Möller et al.*, 2008; *Campos et al.*, 2013]. Both water masses meet at the Subtropical Shelf Front (STSF), a density compensated salinity and temperature front located along the outer shelf between ∼ 33° and 35°S (Figure 1) [*Piola et al.*, 2000, 2008a].

Our knowledge of the circulation patterns over this large shelf region is limited by the scarcity of direct observations. There are only few documented descriptions of current meter time series on the shelf, each lasting only a few months or less [*Rivas*, 1997; *Castro and Miranda*, 1998; *Zavialov et al.*, 2002]. Circulation

patterns over the shelf have been therefore indirectly inferred from hydrographic observations [*Piola et al.*, 2000; *Lucas et al.*, 2005; *Piola et al.*, 2008a, 2008b; *Möller et al.*, 2008] and from regional-scale numerical simulations [*Pereira*, 1989; *Simionato et al.*, 2001; *Ghisolfi and McKee*, 2003; *Palma et al.*, 2004a, 2004b, 2008; *Soares et al.*, 2007; *Combes and Matano*, 2014; *Matano et al.*, 2014, hereafter M14]. These studies indicate that, between 43°S and 38°S, the shelf circulation is generally northeastward, with a maximum during autumn and a minimum during spring. Farther north (between 38°S and 28°S), the shelf circulation is generally southward over the outershelf (dominated by the BC), with seasonal changes in the inner and middle shelf that are followed by significant anomalies of the temperature and salinity fields. During autumn and early winter, the thermohaline structure of the shelf is modulated by SASW advected northward from the south and fresh RdlP water. During summer, there is advection of STSW from the north and local coastal upwelling driven by northeasterly winds. There is also a contribution of South Atlantic Central Water (via the BC) due to shelf-break geostrophic upwelling [*Campos et al.*, 2000; *Palma and Matano*, 2009]. The seasonal variability of the salinity structure is dominated by the migrations of the RdlP plume, which reverses direction following the seasonal changes in the wind [*Piola et al.*, 2008a]. The seasonal changes of the inner and middle shelf circulation are primarily driven by the alongshore component of the wind stress in the inner and middle shelf. Northward winds in winter generate a positive sea level coastal anomaly and a geostrophically balanced northward flowing coastal jet that extends as far north as 29°S during autumn and winter. The freshwater discharges from the RdlP strengthens the inner-shelf and middle-shelf northward jets during autumn and early winter. Upwelling forced by southward winds during spring and summer create a depression of sea level next to the coast and the formation of a southward coastal flow.

The seasonal changes of the circulation over the outershelf are greatly influenced by contiguous western boundary currents and their confluence [*Matano et al.*, 2010; *Combes and Matano*, 2014, hereafter CM14]. Observations and models indicate that the BMC move north to near 37°S in spring (September–December) and southward to ∼38.5°S in late summer and autumn (March–April) [*Olson et al.*, 1988; *Matano et al.*, 1993; *Wainer et al.*, 2000; *Goni and Wainer*, 2001]. This seasonal migration of the BMC is primarily a response to decreases and increases in the strength of the BC during winter and summer, respectively. Although there is a seasonal change in the transport in the MC, it affects the offshore half of the MC, while the location of the BMC is determined more by the strength and position of the BC and the inshore half of the MC, which demonstrates little or no seasonality [CM14].

The northward, downwelling favorable winds in winter create northward currents and onshore Ekman transports that trap the fresher water from the RdlP next to the coast. Relaxations of the winter winds allow some of the fresh water to leave the shelf in filaments that extend into the BC. The waters in these filaments mix with the western edge of the southward BC before being carried offshore in the BMC [M14, *Guerrero et al.*, 2014, hereafter G14]. During summer, poleward winds create upwelling and poleward currents, causing water to move south and offshore. Thus, RdlP plume water moves more directly offshore and into the BMC in summer [M14, G14].

1.2. Contributions From Altimeter Analyses
Altimeter observations offer several new pieces of information and perspectives in relation to the background described above.

1. *Observations of synoptic 2-D surface circulation fields*: Previously published depictions of the temporally varying 2-D surface circulation fields have been derived from numerical model studies. These are validated by comparison to sparse hydrographic surveys and scarcer current measurements in the region [*Palma et al.*, 2004a, 2004b, 2008; CM14, M14]. The altimeter fields provide the first systematically collected, nearly synoptic observations of these Eulerian fields. In addition, we demonstrate that the altimeter fields compare relatively well with the model fields, increasing our confidence that both models and altimeter fields provide a more detailed and consistent picture of seasonal changes in the shelf circulation than previously available.

2. *Onshore-offshore transports*: Altimeter data are used to look at the seasonal patterns of cross-shelf geostrophic surface currents at the edge of the shelf. These are related to model tracers and SSS fields, along with the satellite-derived SSS fields analyzed by G14. The goal is a better understanding of the processes that move water from the shelf into the deep ocean.

3. *Quantification of wind versus steric forcing*: One mechanism responsible for changes in SSH and surface geostrophic currents caused by gradients in SSH is through wind-driven coastal and offshore upwelling/

downwelling. An examination of the statistical connection between wind stress and SSH is presented using the method of Principal Estimator Patterns (PEPs). This allows us to find the amount of variance explained by correlated patterns of the wind and surface height fields. Another mechanism by which the SSH fields can be changed is through thermal expansion and contraction, due to local surface heating and cooling. This is referred to as a "steric" change in height and is often considered a nondynamic effect, although it causes surface currents if it creates gradients in surface height.

The contributions of steric changes and wind stress to height variability is investigated by *Saraceno et al.* [2014] using altimeter SSH data in the SW Atlantic Ocean region between 39° and 27°S, similar to our region of interest. Their focus is on the variability in SSH on multiple time scales, whereas our emphasis is on circulation on seasonal time scales. To look at the seasonal cycle of SSH, they regress gridded SSH fields onto annual and semiannual harmonics, reconstruct SHA from the two harmonic representation and then calculate empirical orthogonal functions (EOFs) of those fields. Only two modes of variability can be determined from this procedure and they identify the first as due to the seasonal heating and steric expansion of the water column, responsible for most of the annual SSH signal everywhere except next to the coast out to midshelf north of the RdlP. The second annual mode is responsible for the signal in that northern coastal and midshelf northern region, which they attribute to a wind-driven dynamic signal. We compare their results to ours in the Discussion section.

2. Data and Methods

2.1. Altimeter Along-Track and Gridded SLA Data, MDT, and ADT

Altimeter data come from two sources: Along-track altimeter sea level anomaly (SLA) height data are obtained from the RADS (Radar Altimeter Database System, http://rads.tudelft.nl/) web site. We use the final research-quality along-track SLA data and the various environmental "corrections" used to construct those data. Included are the tidal corrections, which are estimates of the SSH signals corresponding to all of the tidal components. We analyze these separately, in order to evaluate whether the errors in the tidal corrections are affecting our results (see Appendix A). The along-track data are only used in the analysis of the tidal corrections. Our primary focus is on the seasonal circulation patterns, which we investigate using gridded altimeter SLA data from the AVISO (Archiving, Validation, and Interpretation of Satellite Oceanographic data) site, http://www.aviso.altimetry.fr. Along with the gridded $1/4°$ SLA data set, we also examine the temporally static mean dynamic topography (MDT) data set.

The term "anomaly" in SLA refers to the fact that a temporal mean for the period under consideration is removed at every grid point in an altimeter data set to form the temporal "anomaly," which retains all of the temporal variability of the original data set. The mean SSH that is removed includes both the MDT that is associated with the temporal mean geostrophic surface currents and the nondynamic geoid—the surface followed by an ocean at rest, as it varies with spatial changes in the gravitational field. To create fields of absolute surface geostrophic currents and absolute dynamic topography (ADT), we need to add an estimate of the MDT to the SLA. We use the MDT from the model of M14, after comparing the model MDT to the AVISO estimate of the MDT, as discussed below.

2.1.1. RADS Along-Track SLA Fields

The sea level anomaly for Topex/Poseidon, Jason-1, and Jason-2 data are constructed using the RADS (2012) default corrections, including the GOT4.8 tide model. The altimeter range, orbit, and environmental corrections are tested for extreme values; outliers are replaced with a smoothed version from nearby data. This is similar to the editing employed at the Centre de Topographie des Oceans et de l'Hydrosphere (CTOH) [*Roblou et al.*, 2011; *Liu et al.*, 2012]. The resulting value of the (range–orbit—mean sea surface) is tested using the along-track mean and standard deviation; any remaining extreme values (greater than 4 standard deviations) are removed.

The SLA data from individual cycles are then interpolated to a regular along-track grid with an approximate interval of 7 km. The along-track total tide correction includes the pole tide and solid earth tides as well as the GOT4.8 ocean and load tides. When the analysis period includes the overlap of altimeter missions along the same tracks during the calibration phase of new altimeters, the SLA used during the overlap period is a weighted mean of the two altimeters, with the contribution from each altimeter based on the time since the beginning and end of the overlapped period for each mission.

2.1.2. Mapped AVISO Fields

Mapped SLA anomaly data from altimeters were obtained from AVISO's 2014 reprocessing. We use the $1/4°$ SSALTO/DUACS Delayed Time "Updated" weekly time series of the mapped data (DT2014). This version includes data from all available altimeters at any given time, improving the spatial resolution. We use data from the 12 year period, 2001–2012, during which the number of altimeters with exactly repeating orbits is greatest: four altimeters during three years (October 2002 to September2005) and three altimeters during another six and a half years (January 2001 to September 2002, October 2005 to September 2008, February 2009 to September 2010). During the last two years of this period, the one or two exactly repeating altimeters are augmented by data from altimeters in non-repeating or slowly repeating orbits.

2.2. Wind Data
2.2.1. ECMWF Wind Stress Fields

Wind stress is calculated from the ERA-Interim ECMWF model at approximately 2/3° resolution (http://apps.ecmwf.int/datasets/), using a constant drag coefficient. These are the primary wind forcing fields used in our analyses. An "alongshore" component of the wind stress is defined to lie parallel to a line roughly parallel to the coastline, 38° clockwise from north.

2.2.2. Scatterometer Climatological Wind Stress Fields (SCOW)

The Scatterometer Climatological Wind Stress Fields [*Risien and Chelton*, 2008] are from the SCOW website (http://cioss.coas.oregonstate.edu/scow/). These updated fields cover the complete QuikSCAT period, September 1999 to October, 2009. Since they cover a different period than the SLA data, they are used primarily to confirm the patterns derived from the ECMWF data.

2.3. ROMS Model Mean Surface Height and Geostrophic Velocity Fields

Monthly mean and 12 year mean surface heights for 2001–2012 from the ROMS model of M14 at a resolution of 1/24° are used. The data are interpolated to the $1/4°$ AVISO mapped SLA grid locations and geostrophic velocities are calculated from the model SSH fields as described below for the gridded SLA data.

2.4. Methods: Geostrophic Calculations
2.4.1. Cross-Track Velocities

Velocity anomalies normal to altimeter tracks are constructed from the along-track SLA using an approximately 70 km centered difference followed by a Loess filter with a half-span of 50 km. The velocity from the along-track total tide correction is calculated using an identical 70 km difference procedure and smoothing.

2.4.2. Gridded Geostrophic Vector Velocities

Geostrophic velocities are calculated from the AVISO mapped SLA data and from the ROMS model surface heights using a 3 pt centered difference on the AVISO $1/4°$ map grid. Transects approximately perpendicular to the coast line are constructed at $1/4°$ intervals and the mapped u and v geostrophic velocities are interpolated to the transect locations. The component of the velocity normal to the transect is used as the alongshore component of the velocity and the component parallel to the transect is considered the cross-shelf velocity. The means of the cross-shelf velocities on adjacent transects at the locations nearest the 200 m isobath are fit to four annual harmonics to form seasonal cycles of cross-shelf velocity at the shelf break.

2.5. Methods: Seasonal Cycles: Mean Monthly and Harmonic Analysis

At each grid point, geostrophic velocities are calculated using centered differences. Monthly means of the calendar months are formed over the 12 year period and also from fits of up to four seasonal harmonics (periods of 12, 6, 4, and 3 months). For the harmonic reconstructions, the monthly (seasonal) fields are the sum of the harmonics at the midpoint of the month (season). The results presented here are from the climatological monthly means, which are nearly indistinguishable from the harmonic reconstructions.

2.6. Methods: EOFs and PEPs

Empirical Orthogonal Functions (EOFs) are calculated from monthly time series of mapped wind stress and SLA. The time series of the EOFs are smoothed with a five point boxcar filter before their presentation and discussion. The first three EOFs of alongshore wind stress and SLA are combined using the method of Principal Estimator Patterns (PEPs) to define the pattern of wind stress that has the greatest skill (percent variance explained) in predicting the patterns of SLA, as represented by the SLA EOFs [*Davis*, 1977, 1978; *Strub et al.*,

1990]. The individual EOFs and the PEPs provide evidence for the degree to which the seasonal changes in circulation are driven by winds.

3. Results

One of the reasons that altimeter data have not been analyzed over wide shelves such as found in the SW Atlantic Ocean is the concern that errors in the tidal models contaminate the data in these regions. *Saraceno et al.* [2010] provide evidence that the tidal models in this area agree well with tidal components as estimated from coastal tide gauges. In addition, *Ruiz Etcheverry et al.* [2015] show that root mean square errors between the annual cycles calculated from altimeter and tide gauge data are lower than 2.1 cm in the same region. To build further confidence in the altimeter data over this shelf and away from the coast, we have compared the corrected along-track SLA data in the RADS data set with the tidal corrections from the same data set, over the entire shelf (and offshore). The assumption is that errors in the tidal models will cause the "corrected" SLA values to contain some of the signal from the tidal models. These comparisons are described in detail in Appendix A. The net result is that we find no evidence of contamination of the altimeter data over the shelf north of 40°S, with the possible exceptions of the inner mouth of the RdlP and a few locations very close to the coast. In our analyses, we interpret data from south of 40°S and at grid points next to the coast with caution. There are, of course, other sources of errors and noise in the data, the effects of which are reduced by the use of monthly averages over the 12 year period, fits to harmonic functions and the examination of the first several modes using EOF analysis.

3.1. Seasonal Wind Fields

In Figure 2, the large-scale seasonal changes in winds over the SW Atlantic are depicted by summer (January) and winter (July) fields of wind stress from the ECMWF analysis fields, averaged over the same period as the altimeter data. Figures showing all 12 monthly means of ECMWF wind stress are found in supporting information. The ECMWF fields look very similar to the wind stress fields from the QuikSCAT satellite scatterometer, as presented in the SCOW climatology of *Risien and Chelton* [2008]. In addition to the wind stress vectors, Figure 2 includes the alongshore component of the wind stress, where "alongshore" is defined to be in the direction *toward* the northeast (38° clockwise from north). This is a line roughly parallel to the contours of bathymetry north of 43°S.

During austral winter (July), the region south of 30°S is swept by westerlies, with strongest mean wind stress values south of the RdlP outfall. Given the orientation of the coast, pure westerly winds will include an alongshore component toward the equator, creating onshore Ekman transport, downwelling, and raised sea levels next to the coast that are consistent with equatorward geostrophic surface currents. During austral summer (January), winds north of the RdlP reverse to come from the northeast, creating upwelling favorable conditions, low sea levels next to the coast and poleward geostrophic currents. Summer winds south of 41°S remain downwelling-favorable, from the west or northwest, with less seasonal change at the higher latitudes.

The alongshore component of the wind stress in Figure 2 is upwelling favorable over the shelf in summer as far south as 41°S. Maximum poleward values of over 0.05 N m^{-2} are found between 29° and 33°S during October–January. In winter, equatorward (downwelling favorable) alongshore winds occur over the shelf as far north as 30°S during May–July, reaching 25°S in May. The strongest values are in the south. Fields of wind stress curl (not shown) indicate narrow bands of positive and negative values over the shelf next to the coast in winter and summer, respectively, reinforcing the downwelling and upwelling.

3.2. Mean and Seasonal Surface Circulation Over the Shelf

In Figure 3, we present mean monthly maps of SLA and associated geostrophic velocity anomalies over the shelf during 4 months that illustrate the seasonal variation. One prominent aspect of the shelf circulation is the weakness of seasonal variability in the currents south of the RdlP, compared to the currents farther north. Thus, while there are strong alternations in the height fields south of 36°S between April (high) and October (low), there are only two periods with coherent velocity anomalies above 1–2 cm s^{-1} in that southern region. Both are transition periods from the point of view of wind forcing. Equatorward seasonal velocity anomalies are found between 37° and 40°S during April (Figure 3), connected to even stronger velocities farther north. This is the first month with significant downwelling-favorable alongshore winds south of the
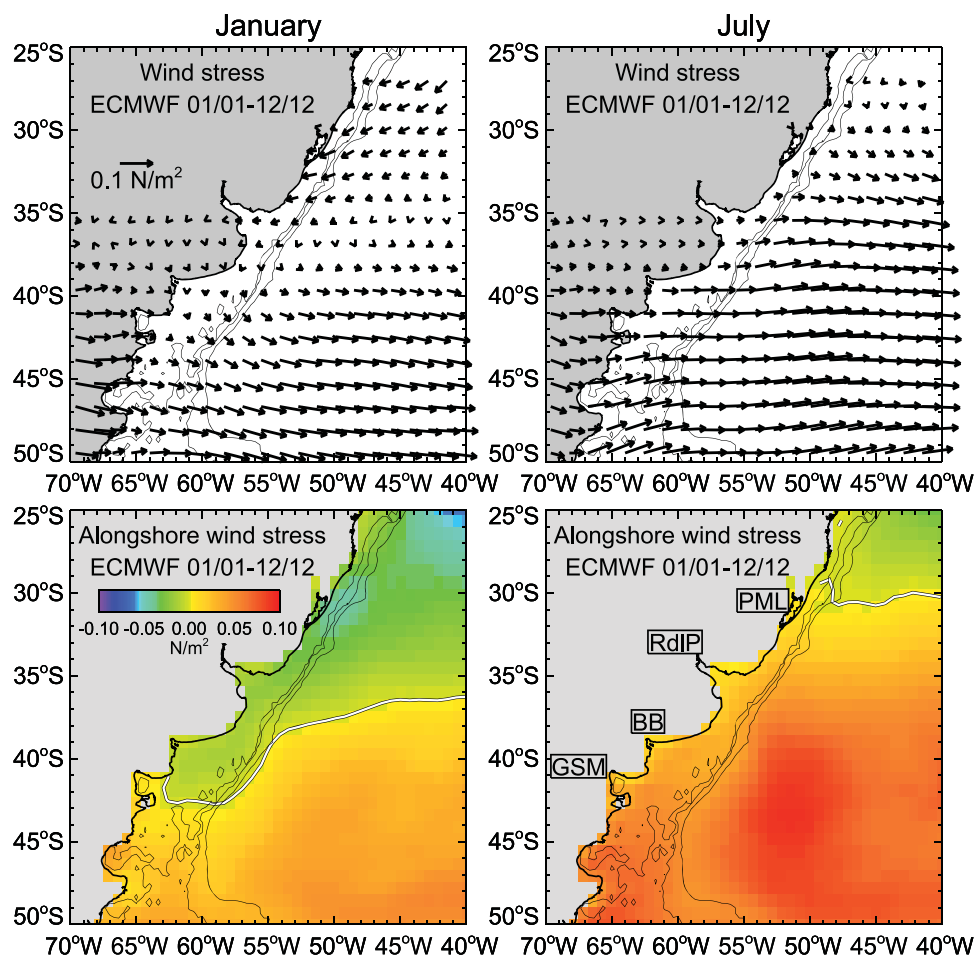
Figure 2. January and July average ECMWF vector wind stress (top) and alongshore wind stress (bottom). The zero alongshore wind stress contour is shown in Figure 2 (bottom). The thin black lines show the 100, 200, and 1000 m isobaths from ETOPO-5. The 200 m isobath is considered to be the shelf break. Locations discussed in the text are shown in the bottom right plot for PML: Patos-Miros Lagoon; RdlP: Rio de la Plata River; BB: Bahia Blanca estuary and El Rincon Bight; GSM: Gulf of San Matias.

RdlP. Likewise, low coastal SLA values and poleward velocity anomalies are found in the same region during August–September (still slightly visible in October), when winds are relaxing but still downwelling-favorable (see the supporting information for the complete set of monthly fields). During other months, current anomalies over the shelf south of the RdlP are mostly negligible.

North of the RdlP, the geostrophic current anomalies display a stronger and more spatially coherent seasonal evolution. The low SLA values and poleward velocities that appear first next to the coast over the broad shelf south of the RdlP in August–September spread to the north of 37°S in October and become the dominant feature between 27°S and 37°S during December–February, as represented by the January mean in Figure 3. When equatorward, downwelling-favorable winds begin in the south during April, high SLA next to the coast and equatorward velocity anomalies appear over most of the shelf domain north of 40°S, retreating to the region north of the RdlP during May–July.

Previous research has shown that the velocity patterns over the shelf are highly influenced by the deep ocean circulation [*Matano et al.*, 2010]. M14 use a high-resolution, dually nested model to investigate the exchanges between the shelf and the deep ocean during the same 12 year period used in our analysis. In Figure 4, we present the mean sea level (MSL) from the M14 model and the mean dynamic topography (MDT, equivalent to the model MSL) from the CNES AVISO web site, which is derived from altimeter and satellite gravity data, along with in situ observations [*Rio et al.*, 2007]. The agreement is generally good, with velocities along the eastern boundary of the shelf in both fields representing the southward BC and northward MC. Near the shelf break, these meet and create offshore flow along the height gradients between
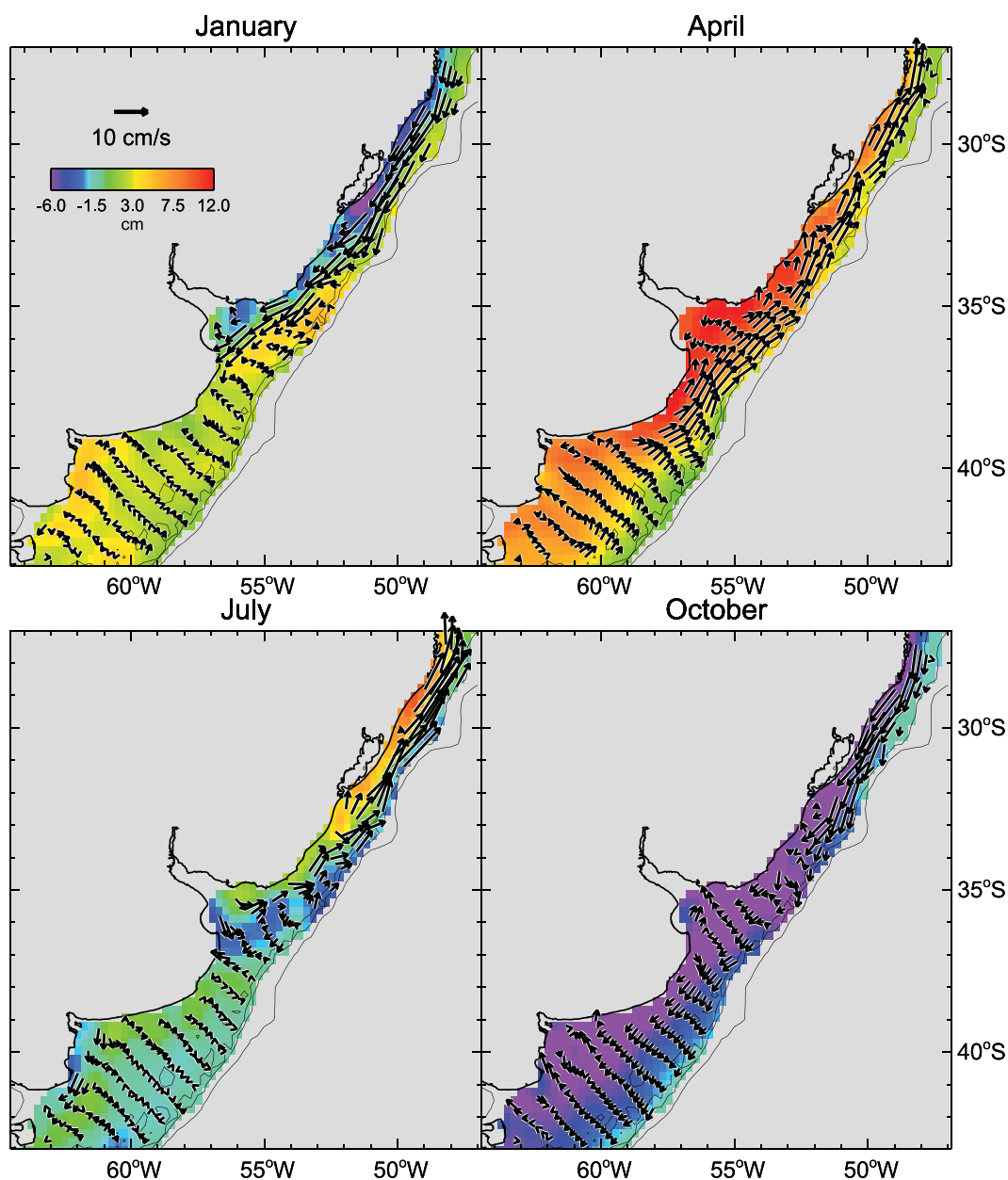
Figure 3. Monthly mean AVISO gridded SLA (color) and associated geostrophic velocity anomalies based on data from January 2001 to December 2012. The isobaths are shown as in Figure 2.

36° and 38°S. Over the shelf, currents are in the same direction as the offshore MC and BC, except between the RdlP and Patos/Mirim Lagoon (32°–37°S). There the equatorward flow over the shelf opposes the poleward flow in the offshore BC, creating a confluence over the shelf near 32°S.

The agreement between the model MSL and the AVISO MDT provides confidence in both fields. To create an estimate of seasonal changes in the absolute dynamic topography (ADT) and the associated absolute geostrophic currents, we add the model MSL to the altimeter SLA. By using the slightly smoother model mean height and surface currents to create the altimeter ADT, the seasonal changes in ADT and associated currents can be directly compared (model to altimeter), without considering differences in the stationary means.

Figures 5a and 5b compare the altimeter and model fields of ADT and absolute geostrophic surface currents. The addition of the seasonal anomalies (Figure 3) to the model MSL (Figure 4) moves the confluence
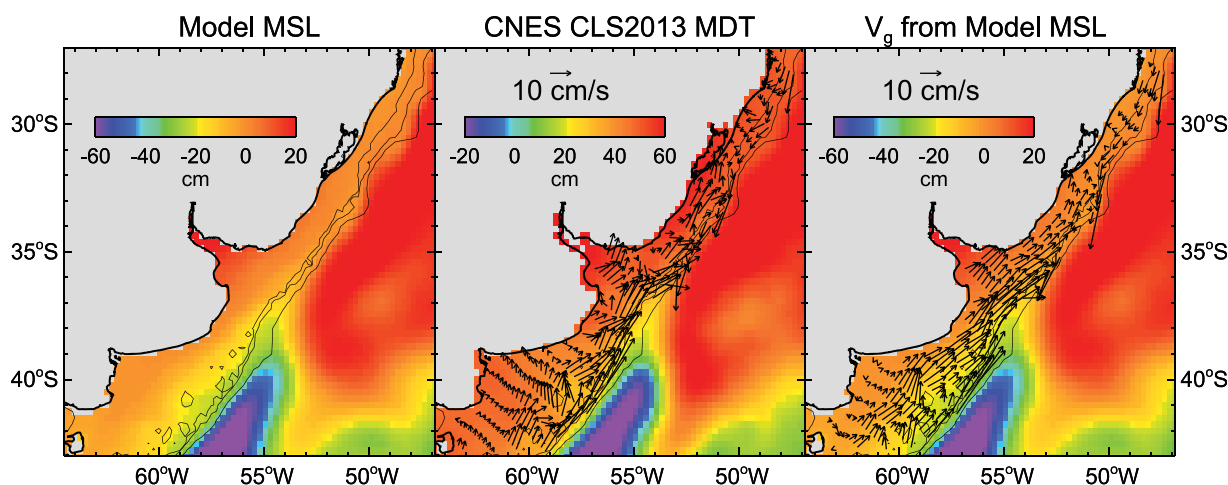
Figure 4. Mean Sea Level (MSL) from the ROMS model of M14 (left), altimeter Mean Dynamic Topography (MDT) from AVISO (middle); and the geostrophic velocities associated with that MDT; and the mean surface geostrophic velocities calculated from the ROMS model MSL over the shelf, overlaid on the same MSL from the left-hand plot (right). Note the offset of approximately 40 cm between model and altimeter mean heights. The model fields are those that are added to the altimeter fields to convert the anomalies of sea level or velocity to absolute values. The isobaths are shown as in Figure 2.

of the shelf currents from its mean position near 32°S to ∼34°–35°S in summer (December–January), back northward in autumn (April) to approximately 27°S, and beyond the northern boundary of our region in winter (July). Given the weak seasonal variability in the altimeter SLA south of the RdlP, the agreement between the model and altimeter fields in the southern halves of Figures 5a and 5b comes mainly from their common mean field. The more assuring agreement is north of the RdlP, where the seasonally varying model and altimeter fields produce similar moving patterns in the location of the confluence between equatorward and poleward currents over the shelf.

3.3. Quantifying Seasonal Wind-Driven Changes in SLA

Figure 6 presents the first EOF modes for alongshore wind stress (top) and AVISO SLA (middle). Approximately 80% of the variance of the alongshore wind stress over the shelf is represented by its first mode (top), with a spatial concentration of the strongest seasonal changes in alongshore wind forcing over the outer shelf in the region between 30° and 37°S. Positive (Equatorward) values occur in austral autumn and winter (April–July), reversing in spring and summer (September–March). The patterns are consistent with the January and July wind stress fields shown in Figure 2 but provide a more detailed view of the monthly and interannual variability. The seasonal cycle demonstrates a rapid transition from upwelling in March to downwelling in April, with a somewhat more gradual return to upwelling between July and October. On individual years, either or both transitions can be quite abrupt and persistent (e.g., 2001) or consist of multiple transitions and reversals (2005, 2010). The decrease in the strength of the alongshore winds closer to the coast is consistent with a coastal band of positive wind stress curl in winter and negative wind stress curl in summer. To address the question of whether the strength of ECMWF winds decrease artificially next to the coast, we repeated the EOF calculation with monthly QuikSCAT winds from the period 2001–2009 and found a similar decrease in the strength of the alongshore wind stress next to the coast between 31° and 37°S. This supports the complementary roles of wind stress and wind stress curl next to the coast in creating upwelling and downwelling conditions in spring-summer and autumn-winter, respectively. The time series for the QuikSCAT EOF (not shown) exhibits an even stronger abrupt transition between March and April and a more gradual reversal between July and October. It also includes most of the extremes found in the individual years for ECMWF winds in Figure 6, including stronger peaks of downwelling in 2002–2003, and 2007–2009 and stronger periods of upwelling (negative spikes) in 2001, 2004, and 2006–2008.

The middle plot of Figure 6 presents the first EOF of the monthly SLA, while the time series in the bottom plot represents the monthly spatial mean of the SLA over the shelf (the shaded region in the map to the left). A comparison reveals nearly identical time series for the first mode of the SLA over the shelf and the spatial mean of SLA over the shelf. The spatial pattern of the first SLA mode includes a cross-shelf gradient,
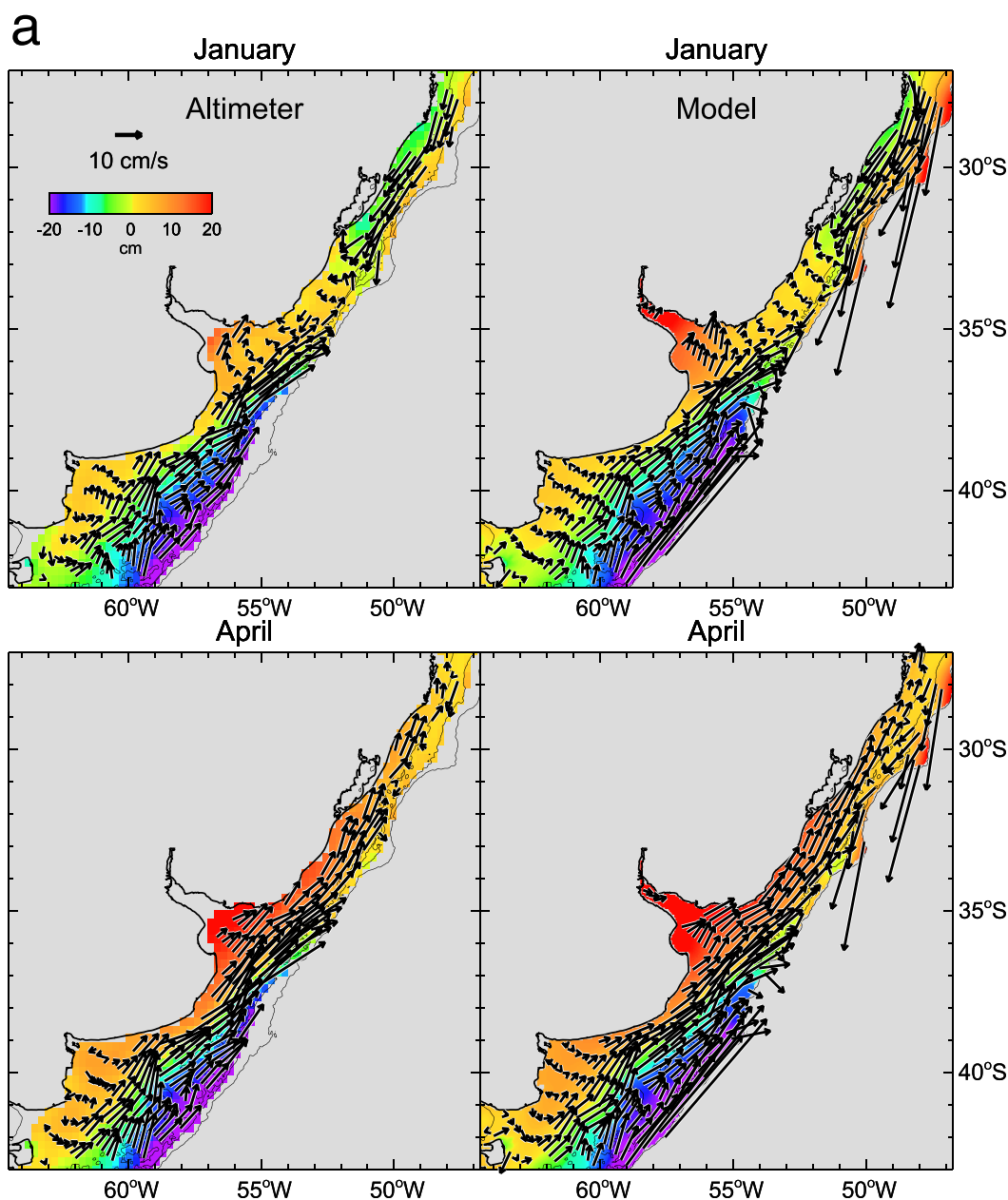
Figure 5a. Representative summer and autumn monthly mean geostrophic surface velocities (vectors) calculated from the monthly mean absolute SSH fields (color) from the 12 year study period. (left) AVISO SLA + ROMS mean. (right) ROMS surface height and geostrophic velocities calculated from that height. The isobaths are shown as in Figure 2. Velocities from slightly farther offshore are included in the model fields, representing the edges of the BC and MC.

with low values near the shelf break and higher values at the coast, concentrated in the middle and southern parts of the region. The contour value of 1.0 is found near midshelf for much of the shelf domain south of 32°S, although it moves to the shelf break around 36°S. The SLA values along this contour rise and fall with values (in centimeter) given by its time series, nearly identical to the 5 cm rise and fall of the spatial mean over the shelf shown in Figure 6 (bottom). For both of these time series, the monthly mean seasonal cycle (in red) rises from a minimum near −5 in October to a value of +3 in February and March and then to a maximum of +6 in April. Multiplying the time series and the spatial function in the middle plot results in a mean SLA rise next to the coast from ∼−8 cm in autumn to + 12 cm during spring and summer.

As seen in Figure 6 (top), winds north of the RdlP are upwelling favorable during October–March, opposing the rise in sea level found at the coast (in Figure 6, middle), although the winds are concentrated north of
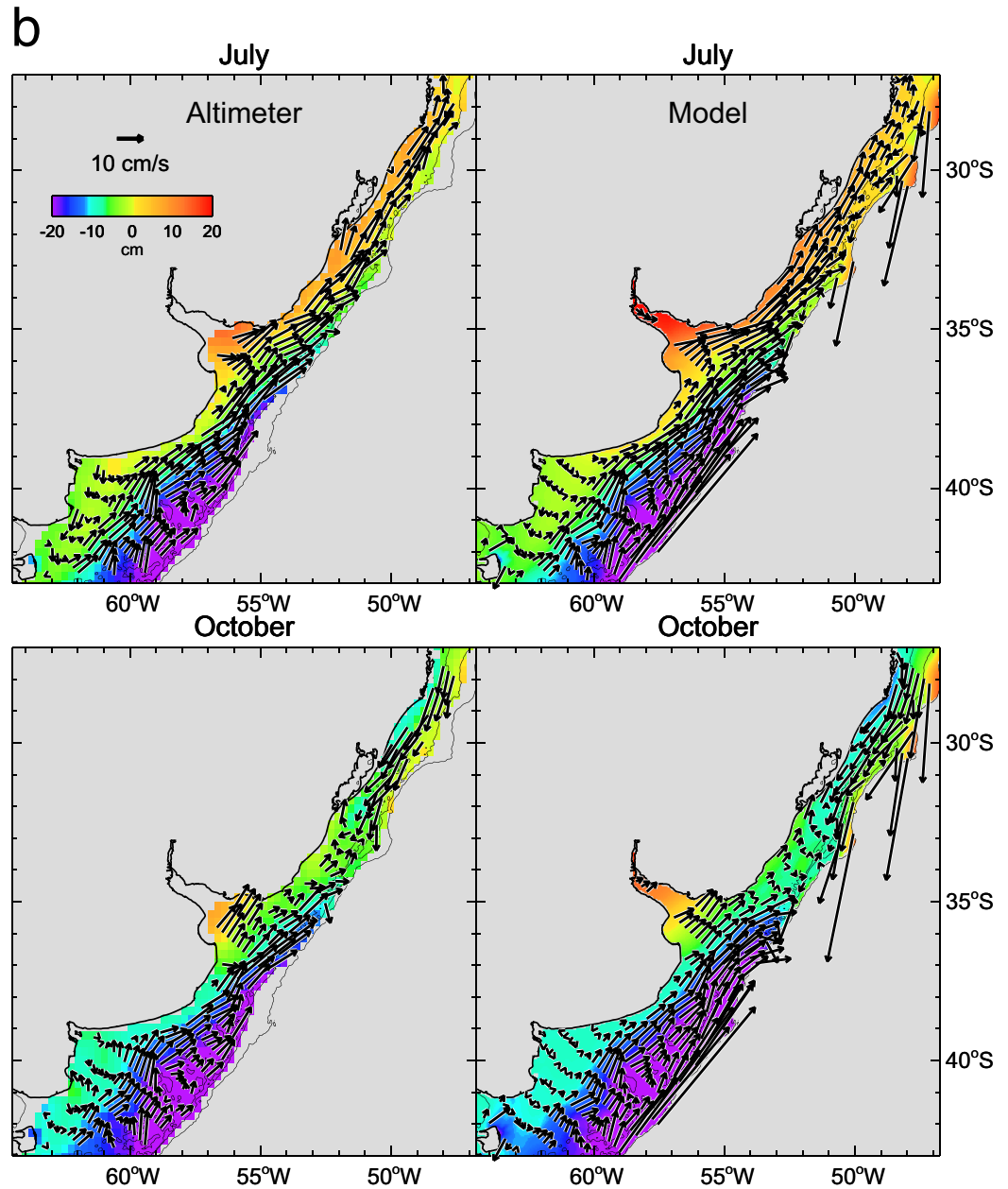
Figure 5b. Representative winter and spring monthly mean geostrophic surface velocities (vectors) calculated from the monthly mean absolute SSH fields (color) from the 12 year study period. As in Figure 5a.

the SLA maxima. The timing of the coastal SLA rise during spring and summer gives it the appearance of a rise in the mean steric height over the shelf, associated with seasonal surface warming and thermal expansion of the upper water column, as commonly found in the large-scale, deep ocean basins. However, the cross-shelf gradient in raw SLA associated with this signal is a dynamic feature, indicating alongshore currents, unlike the usual depiction of a nondynamic uniform steric rise and fall of SLA. We return to the question of steric versus wind-driven responses of the SLA in the Discussion.

To focus on the dynamic SLA gradients, we eliminate any uniform increase or decrease of the mean height in our region by removing the spatial mean of SLA over the shelf for each monthly field (the signal shown in Figure 6, bottom), before carrying out the EOF decomposition. We refer to this as "demeaned SLA" to differentiate it from the "raw SLA" (no spatial mean removed). The first two EOF modes for the demeaned SLA
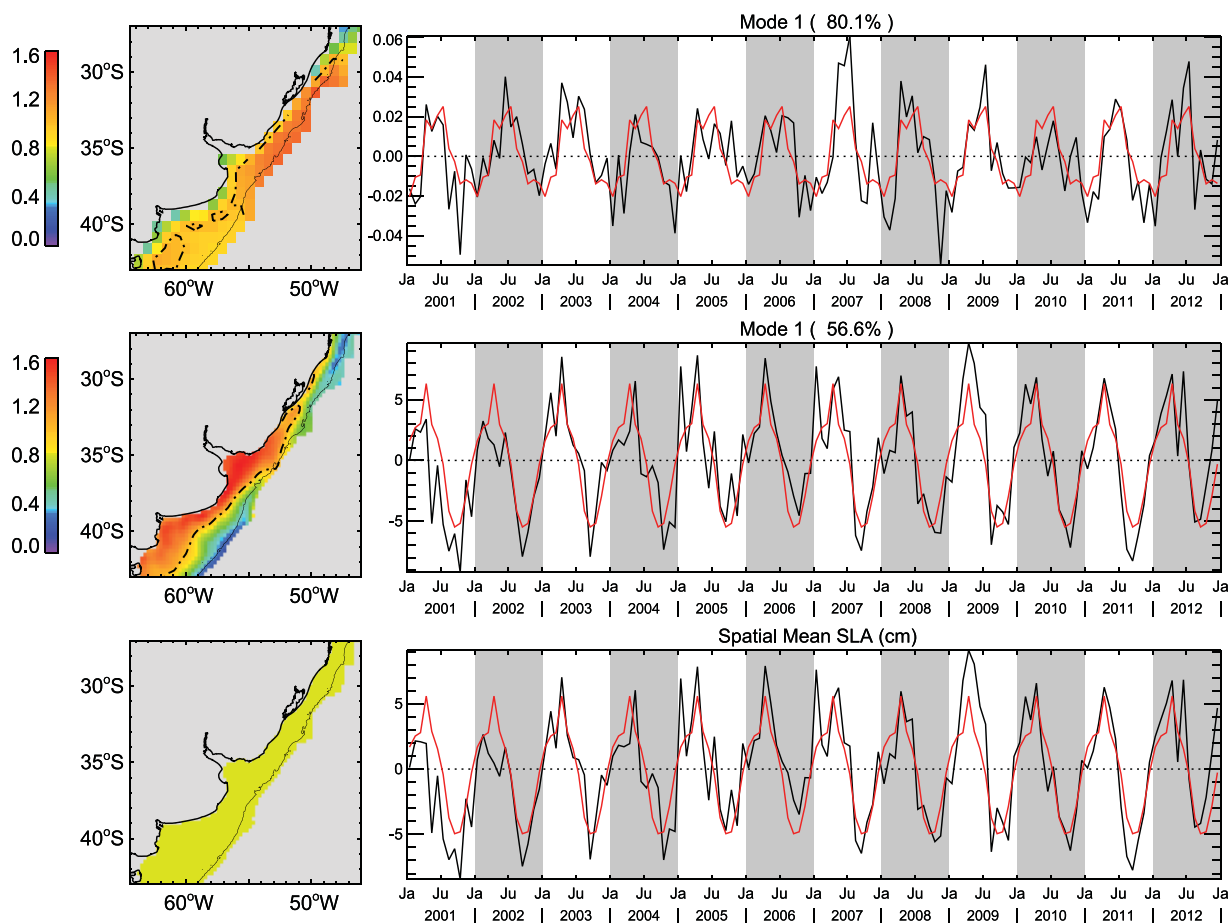
Figure 6. First EOFs of alongshore wind stress (top, explaining 80% of the variance) and SLA over the shelf (middle, explaining 57% of the variance). The bottom plot shows the time series for the mean SLA averaged over the entire shelf (depicted here by the shaded region). The dot-dash line in the top and middle plots is the 1.0 contour. The red lines in the right-hand side plots are the mean monthly seasonal cycles (12 year mean of each calendar month). The 200 m isobath is shown.

are shown in Figure 7. In the first mode's spatial pattern, the cross-shelf gradient of SLA associated with alongshore current anomalies is more concentrated along the zero contour north of the RdlP. The second mode divides the domain into regions north and south of the RdlP, with cross-shelf gradients of SLA (and alongshore current anomalies) of different signs in the two regions. Together, these two modes account for ∼42% of the variance in the dynamical signal.

The mean seasonal cycle of the time series for the first mode of demeaned SLA (explaining 23.5% of the variance) is much more similar to that of the wind in Figure 6 (top). There is a rapid transition from negative values in February to sharp positive values in April (equatorward current anomalies) that persists through July. The transition to negative values (poleward current anomalies) occurs during August–September reaching a negative maximum value in October and continuing with negative values through February. The individual years also show interannual variability in the positive and negative peaks that are similar to those found in the wind time series. The second mode explains 18% of the variance and has positive SLA values north of the RdlP from May through November, with a peak in August–September. The fact that the peaks of the two modes are separated by approximately 3–4 months allows their combination to represent high and low SLA signals that appear first in the south and move to the north, similar to the phase plots for the annual harmonic shown by *Saraceno et al.* [2014].

One point that is not as easily seen in the EOFs of Figure 7 is the weakness of the seasonal variability in surface current anomalies south of the RdlP. It is somewhat indicated by the weaker cross-shelf SLA gradients in the south in the first mode and by the fact that the cross-shelf gradients are of opposite signs in the south for the
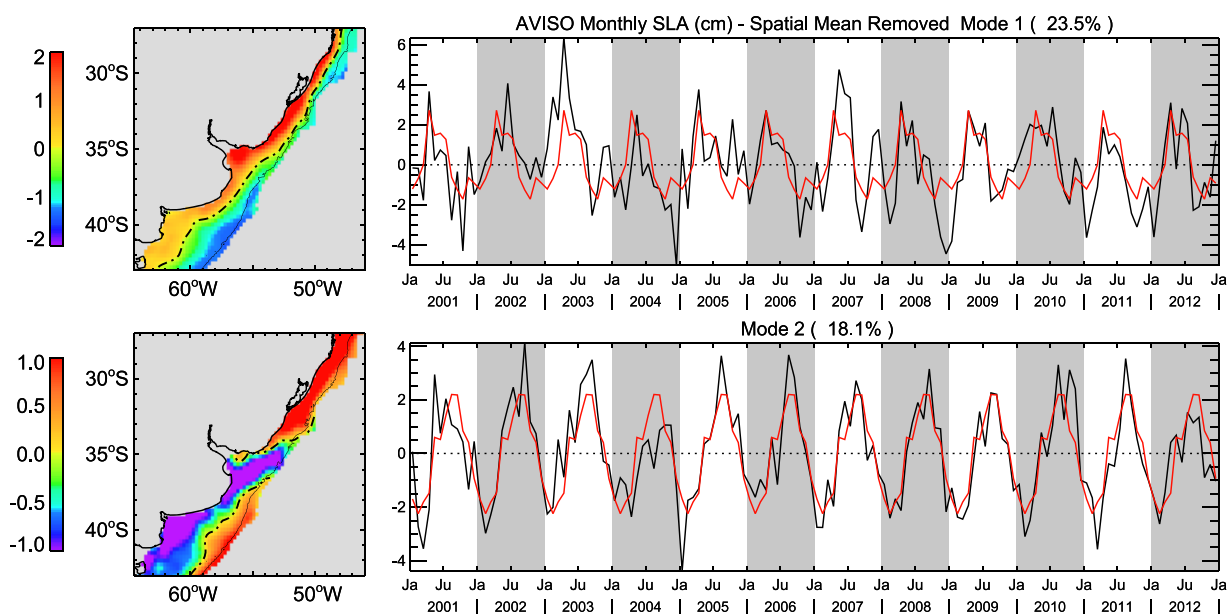
Figure 7. First 2 EOFs of SLA over the shelf, after removing the spatial mean of each monthly field (the spatial mean over the region depicted in the bottom plot of Figure 6). The dot-dash line in the left-hand side plots is the 0 contour. The removal of the spatial mean leaves only the changes in the gradients over the shelf. The first and second EOFs represent 23.5% and 18.1% of the variance in these gradients, respectively. The third EOF (not shown) represents less than 6% of the remaining variance, without a strong seasonal cycle. The red line is the mean monthly seasonal cycle. The 200 m isobath is shown.

first and second mode. When the time series are of the same sign (summer and winter), the velocity anomalies associated with these modes tend to cancel out. They produce significant velocity anomalies only when the time series are of opposite signs. This only occurs during parts of the transition seasons: April and August–December (strongest during August–September). The weakness of the seasonal variability in the current anomalies is much easier to see in the individual monthly means of Figure 3 and supporting information.

To quantify the relation between the wind forcing and SLA response, we calculated PEPs that link the alongshore wind stress and SLA in Figure 8. This method combines the EOFs of the predictor (wind stress) and predictand (SLA) to identify spatial patterns of the predictor that are most highly correlated with the spatial patterns of the predictand's EOFs. A single time series modulates the spatial patterns of both variables. First we use the alongshore wind stress to predict the demeaned SLA and show their time series in Figure 8 (top). This time series and the spatial patterns of the alongshore wind stress (Figure 8, bottom left) and demeaned SLA (Figure 8, bottom middle) are very much like the patterns of their first mode EOFs by themselves in Figures 6 (top) and 7 (top), now explaining 79% of the wind stress and 17% of the SLA variances. Both spatial patterns extend along the entire latitudinal region but are concentrated north of the RdIP, as are their original EOFs.

When the winds are used to predict the response of the raw SLA variance, the process acts differently and does not predict the first mode of the raw SLA (Figure 6, middle) very well. It reproduces only 31% of the original first raw SLA EOF, which was concentrated in the south. Rather, it produces a spatial pattern concentrated in the north (Figure 8, bottom right), similar to that of the spatial patterns of the first mode demeaned SLA (Figure 7, top and Figure 8, bottom middle). The time series and spatial patterns for the wind (not shown) in the PEP that predicts the raw SLA are very similar to those in Figure 8, indicating that the same wind forcing is being selected in each case. The first PEP mode for the wind forcing of raw SLA explains only 58% of the wind variance and 21% of the raw SLA variance (compared to 80% of the wind variance and 57% of the raw SLA variance for their first EOF modes). Thus, use of the wind forcing for both raw and demeaned SLA, picks out almost the same SLA response and identifies it as concentrated in the north, with a time series like the wind and more dynamic demeaned SLA EOFs, rather than like the time series of the raw SLA (Figure 6, middle). The conclusion we draw from these PEPs is that the concentration in the south of the seasonal rise and fall of the raw SLA, represented by the first EOF shown in Figure 6 (middle), is not primarily forced by the wind.
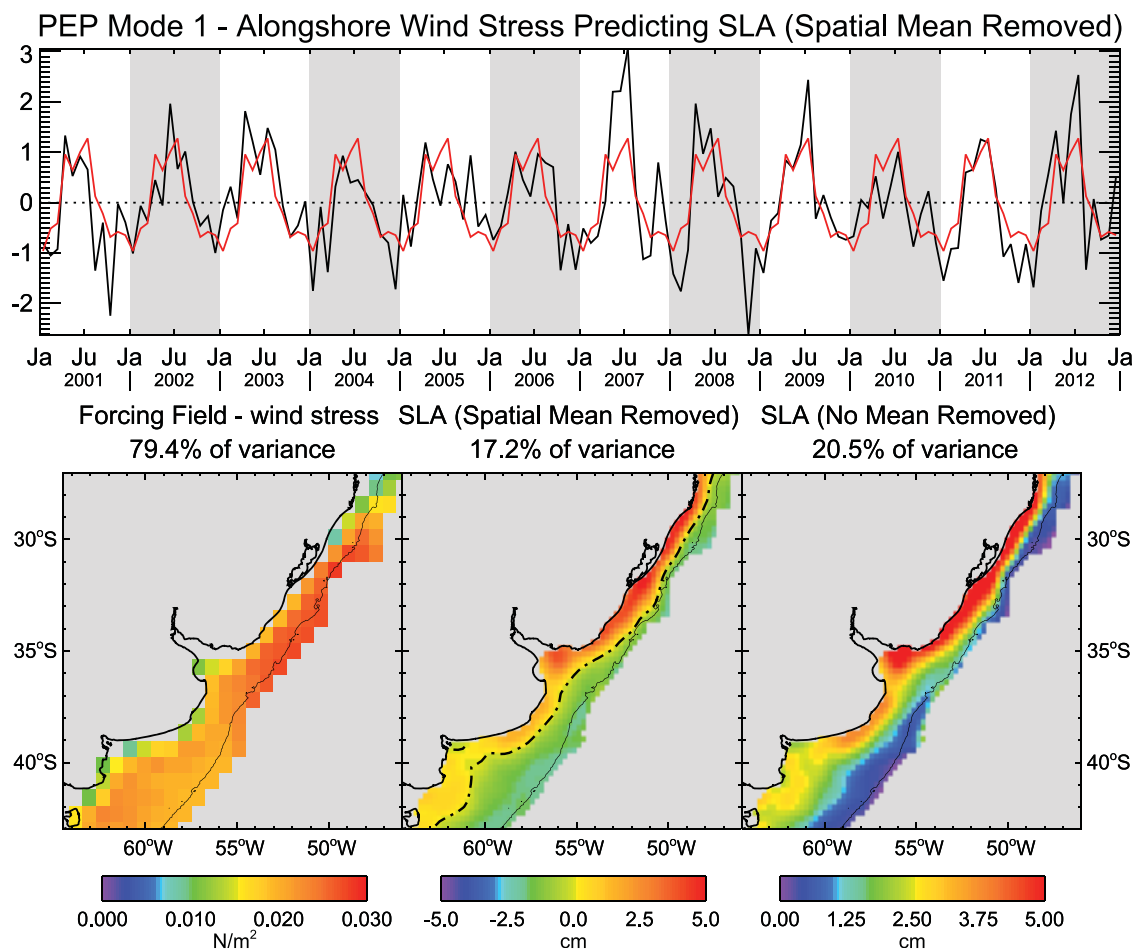
Figure 8. First Principal Estimator Patterns, relating spatial patterns of alongshore wind stress (bottom left, 79.4% of the variance) to those of the SLA after removing the spatial mean of each monthly field (bottom middle, 17.2% of the variance) and SLA without removing the spatial mean (bottom right, 20.5% of the variance). Both bottom left and bottom middle patterns vary with the amplitudes of the time series shown in the top plot. The time series and wind patterns (top and bottom left plots) look nearly identical to their patterns in the PEP that does not remove the mean (bottom right plot). The red line is the mean monthly seasonal cycle (12 year mean of each calendar month).The 200 m isobath is shown.

However, the PEPs also provide evidence that the winds force not only the gradient of the SLA (Figure 8, bottom middle) but also some part of the mean seasonal increase and decrease in height of the raw SLA. This is seen in the spatial range of heights for the PEP of wind and raw SLA (Figure 8, bottom right), which is all of one sign and extends from near zero at the shelf break to maxima of around 5 cm or more at the coast. Using the yellow "contour" to represent the mean over the shelf, the time series combines with the spatial pattern to describe a mean that rises and falls 2.5 cm during winter and summer, respectively, concentrated in the north. We interpret this as a dynamic response to the seasonal changes in alongshore winds and currents, which force mass (and mean sea level) to increase and decrease over the shelf in the north. Thus, about half of the 5 cm rise and fall of the mean SLA over the shelf depicted in Figure 6 (bottom) is wind-driven and not simply a response to seasonal heating and steric sea level rise.

3.4. Cross-Shelf Currents

M14 and G14 investigate the salinity signature of the cross-shelf exchanges in our study region. These studies indicate that relatively fresher waters, associated with the discharges of the RdlP and the Patos/Mirim Lagoon, move to the north over the shelf during winter, mostly contained next to the coast by the onshore Ekman transport driven by equatorward winds. In summer, poleward currents and offshore Ekman transport send the fresh water toward the south and the shelf break, feeding it into the offshore BMC. The altimeter and model fields in Figure 5 show the geostrophic component of the currents over the shelf, confirming
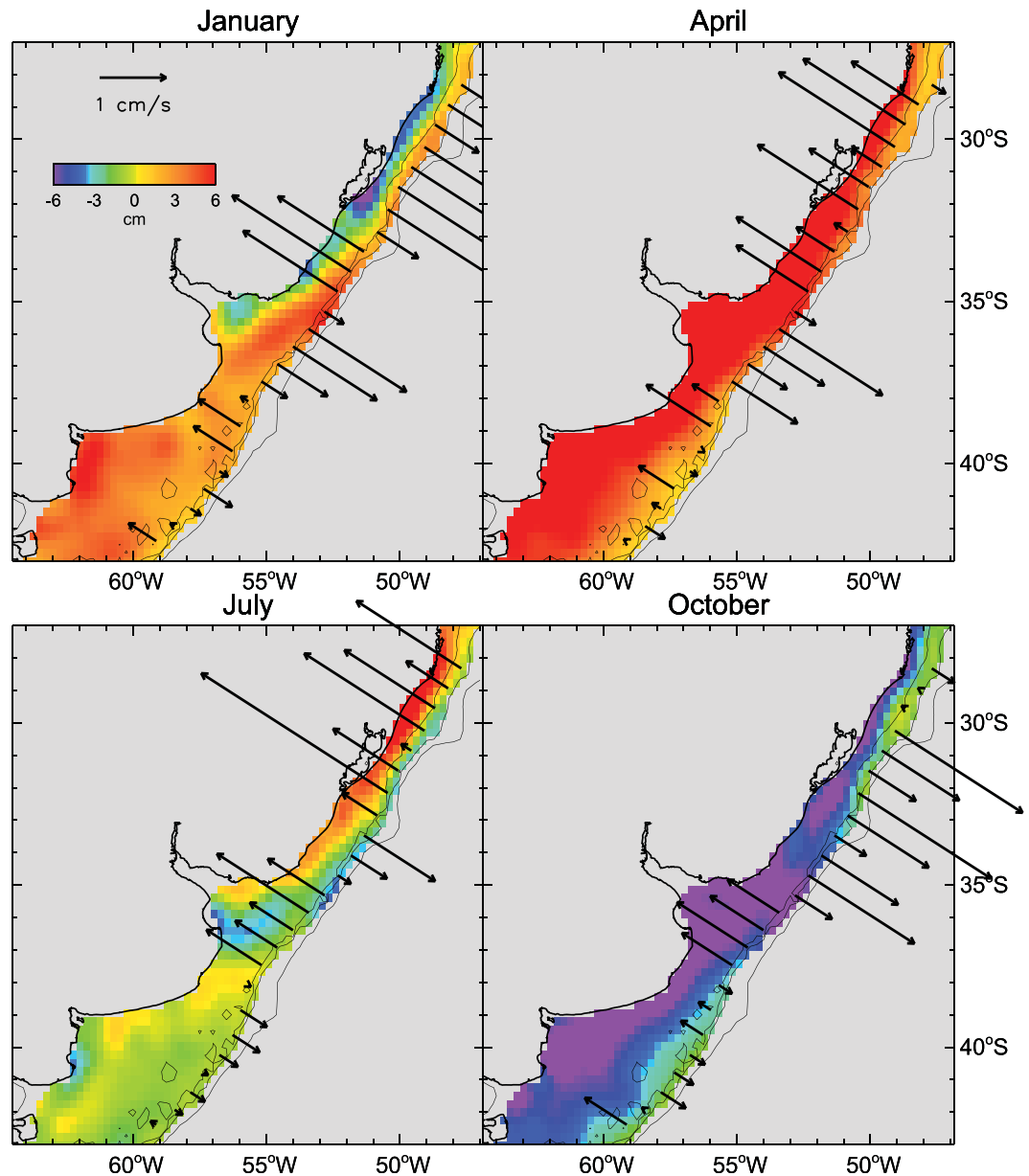
Figure 9. Monthly anomalies of cross-shelf geostrophic velocities at the 200 m isobath associated with AVISO SLA height fields, reconstructed from four seasonal harmonics (periods of 12, 6, 4, and 3 months) from the 12 year study period. The isobaths are shown as in Figure 2.

the alongshore alternation of the currents north of the RdlP. They also hint at an onshore-offshore component of the circulation at the shelf break.

A further refinement of the analysis is used to look more explicitly at the temporally varying offshore transport, considering only the geostrophic component that can be revealed by the altimeter data. The monthly gridded geostrophic velocity anomalies are first calculated from the AVISO gridded SLA fields (the same velocities used to form Figure 3). These are interpolated to the shelf-break, as represented by the 200 m isobath. We then calculate the onshore-offshore component of these velocity anomalies and fit these to four annual harmonics to represent the seasonal cycle of cross-shelf surface current anomalies in Figures 9 and 10. We note that reconstructions of the cross-shelf velocity anomalies from EOF analysis (using three or four EOFs) produce similar fields as the fit to harmonics. Both methods help to reduce noise in the weak cross-shelf velocity anomalies.

Seasonal U (Harmonics) from Altimeter SSH 2001-2012
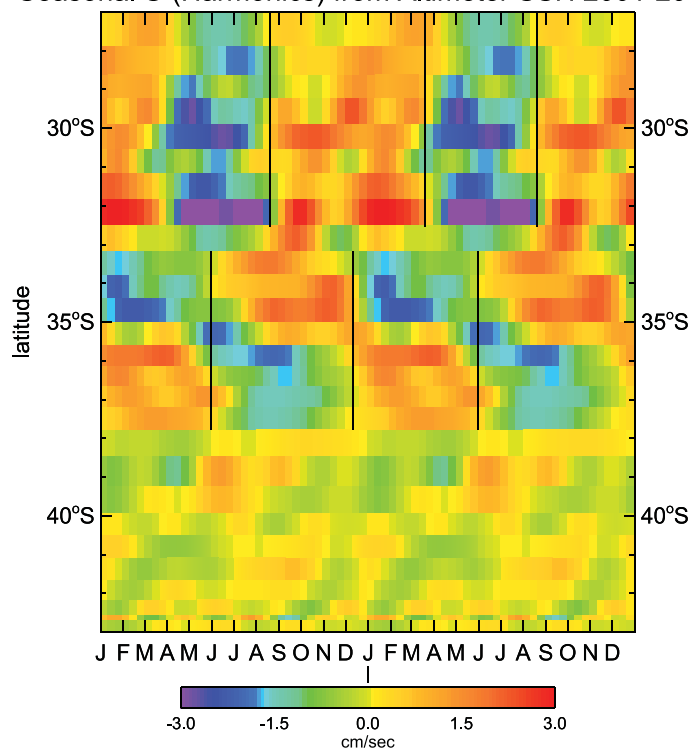
Figure 10. Seasonal geostrophic cross-shelf surface velocity anomalies at the shelf-break (200 m isobath), as reconstructed using 4 harmonics. Positive (red) velocities indicate offshore flow.

The vectors in Figure 9 represents only the temporal variability in the cross-shelf velocity anomalies (like Figure 3), superimposed on the same SLA fields as found in Figure 3 (with a different color bar); no long-term mean has been added. An examination of cross-shelf flow anomalies during the individual months is presented in a time-latitude diagram in Figure 10. The strong patterns occur north of 37.5°S, where there are three distinct regions. Offshore of the mouth of the RdlP (35.0°–37.5°S), current anomalies are offshore during summer-autumn (December–May) and onshore during winter-spring (June–November). North of the RdlP (32.5°–35.0°S), the opposite pattern is found and this is delayed by 2–3 months farther north between 27° and 35°S. Thus, offshore flow anomalies start between 32.5° and 35.0°S in June and extend northward beyond 32.5°S in August. This reverses to onshore flow anomalies between 32.5° and 35.0°S during December–January, which extend north of 32.5°S during March–April. When the model MSL is added to the altimeter SLA (not shown), the offshore absolute geostrophic flow between 34° and 37.5°S (the RdlP mouth) remains all year, maximum in summer-autumn and minimum in winter-spring. North of the RdlP, the cross-shelf flow anomalies continue to change direction seasonally, modified in strength but unchanged in direction from the patterns described above.

4. Discussion

The aspect of our analysis that sets it apart from most others is that it is based on a set of consistently collected observations with uniform coverage over the continental shelf during a period of 12 years, during most of which there were 3–4 altimeters in operation. Our work extends the efforts of *Saraceno et al.* [2014], who examine the altimeter height fields, whereas we focus on the geostrophic surface currents associated with the dynamical gradients in those heights. Below, we compare the altimeter-derived descriptions of seasonal changes in the alongshore and cross-shelf surface currents to previous observational and model studies. Previous discussions of the circulation fields as inferred from hydrographic data include those of *Piola et al.* [2000]] *Lucas et al.* [2005], *Piola et al.* [2008a] and *Möller et al.* [2008]. Realistic model simulations of the circulation are those of *Palma et al.* [2008], CM14 and M14.

4.1. Is the Geostrophic Balance a Valid Assumption?

By using the height fields to calculate seasonal changes in the circulation, we raise an initial, basic question: "Can we expect the dominant currents to be well represented by geostrophic calculations made from the altimeter or model heights?" *Palma et al.* [2008] discuss the dynamical balances of realistic model simulations for cross-shelf transects at 32°–33°S and 38°S. For alongshore currents, the vertically integrated momentum balance is in geostrophic balance over the entire shelf and slope. For the cross-shelf component of the current, they only present the balances for the bottom boundary layer at 32°–33°S, where the vertical friction term plays a role over the outer shelf and slope, but is near zero at the shelf-break, creating an approximate

geostrophic balance. In addition, their unpublished results demonstrate that the vertically-integrated cross-shelf velocity is also nearly geostrophic. Other terms in the momentum budget are significant but cancel out. In the surface layer, that balance is almost purely geostrophic—the pressure and Coriolis terms dominate and are in balance, while other terms are negligible. This is especially true near the shelf break, which is where we calculate the geostrophic cross-shelf currents. Thus, we accept the geostrophic balance as valid to estimate alongshore currents over the shelf and cross-shelf currents at the shelf break.

An additional question is whether the surface geostrophic currents represent the entire water column, or if vertical shears diminish or reverse the currents deeper in the water column. We do not think this is a problem for the alongshore velocities. The sections shown by *Palma et al*. [2008] include shears but only minor reversals in bottom boundary layers along sections at both 32°–33°S and 38°S, indicating that the geostrophic surface currents may overestimate the integrated currents but do not misrepresent the direction of the flow. Since geostrophic currents calculated from altimeter heights are most representative of currents just below the Ekman depth [*Strub et al*., 1997], which should be around 30–50 m, we consider the geostrophic velocities calculated here to represent the upper water column, overestimating the deeper velocities. For the cross-shelf velocities, we are less certain of the ability of the geostrophic velocities to represent the currents over the shelf in the upper stratified ocean during summer. This is especially true over the inner shelf, where strong vertical shears and current reversals have been documented across a turbidity front that separates the inner and outer RdlP estuary, at depths of approximately 10 m, over 100 km inshore of the shelf break [*Framiñan et al*., 2008]. Our interest, however, is at the shelf break. *Möller et al*. [2008] and *Piola et al*. [2008a] show that surface heating creates a strong thermocline between 30 and 50m depth in summer over the shelf; *Piola et al*. [2008a] emphasize that the transports in the upper, stratified ocean during summer create isopycnal connections between regions on either side of the Subtropical Shelf Front (STSF), which stretches from south to north near the shelf break. How well the geostrophic currents represent these transports remains an open question.

4.2. Seasonal Variations in Shelf Circulation

Piola et al. [2008a, 2008b] and *Palma et al*. [2008] show a stronger and more rapid onset of the equatorward flow in autumn, with a more gradual reversal to poleward flow in spring and summer over the inner and middle shelf north of the RdlP. These observations and model results are similar to what we see in the seasonal transitions in alongshore wind stress (Figure 6) and demeaned SLA (Figure 7). North of the RdlP during the winter equatorward flow, the modeling studies and hydrographic analyses depict a relatively barotropic inner half of the shelf and a more stratified outer shelf, with salinity controlling the density. Just offshore of the shelf break, the southward BC carries Tropical Water to the south, where it meets the BMC near 38°S [*Möller et al*., 2008]. South of the RdlP, the model circulation of *Palma et al*. [2008] also includes southward flow during winter along the outer shelf and the development of an anticyclonic gyre in the inner shelf region of the El Rincón Bight (~39°S–40°S, offshore of BB). In summer, the upper 50 m are strongly stratified by temperature, due to surface heating, with cross-shelf connections stretching across the STSF. North of 33°–34°S, the flow reverses to become southward. Near the RdlP and farther south, *Lucas et al*. [2005] describe more periodic summer relaxations and reversals of the northward flow. Opposing the poleward flow, a tongue of Subantarctic Shelf Water (SASW) extends to the north along the outer shelf past the mouth of the RdlP to 34°S or 33°S, separating fresher Plata Plume Water on the inner shelf from STSW next to the shelf break.

In the southern half of the domain, the altimeter analysis shows a generally weak seasonal variability that contrasts somewhat with the reversals in flow noted by *Lucas et al*. [2005]. The altimeter velocity anomalies are poleward in August–October over midshelf south of the RdlP (Figure 3 and supporting information), consistent with weakening of the northward flow in late winter and spring, although this does not produce a reversal in the absolute monthly mean flow during those months (Figure 5 and supporting information). It is possible that the geostrophic calculations miss a reversal in the upper ocean that carries the fresher salinities back to the south during this time, while deeper currents remain northward. The altimeter-derived velocity fields are in better agreement with the model results of *Palma et al*. [2008], which show a general northeastward flow all year south of the RdlP, strengthening in autumn and weakening during spring. In the El Rincón Bight, there is an indication of an increase in the altimeter SLA field in July (Figure 3), consistent with a strengthened of anticyclonic flow in that region as found by *Palma et al*. [2008], although the altimeter's resolution is not sufficient to show a complete gyre.

Offshore of the RdIP and farther north, the altimeter analysis is in agreement with the more rapid transition in alongshore flow in autumn and more gradual transition in spring and summer (Figures 6–8), indicating this as a robust feature of the wind-driven system. The SLA gradients associated with seasonal changes in the velocities are also stronger in the northern half of the region (Figures 7 and 8). In winter, the hydrographic data show that northward winds drive a narrow coastal band (∼50km wide) of northward-flowing fresh waters from the RdIP and PML, extending as far north as 27°S [*Piola et al.*, 2008a]. *Piola et al.* [2008b] estimate the speed of the northward current as 150–300 km/month (5–10 cm s^{-1}). Figure 3 shows the April altimeter-derived geostrophic anomalies of northward currents extending from 43° to 27°S, a pattern that continues between 36° and 27°S during May–July. Combined with the mean fields in Figure 4, the absolute velocities calculated from both the altimeter and M14 model heights are also northward over most of the coast during April–July, with magnitudes of ∼10 cm s^{-1} (Figure 5 and supporting information). There is thus good agreement between the wintertime alongshore circulation fields estimated from the altimeter, model and hydrographic in situ data.

The slow reversal of the altimeter-derived northward current anomalies and absolute mean currents occurs during August–January. In Figure 3, it is notable that January southward geostrophic current anomalies are only southward as far as 36°–37°S, while in Figure 2 summertime alongshore winds over the shelf are southward as far as 41°–42°S. In addition, the southward current anomalies are weak along the outer shelf south of 33°S. The net result is that the January absolute geostrophic surface velocities in Figure 5 are only southward along the inner shelf as far south as 35°S, while remaining slightly northward along the outer shelf as far north as 34°S. This is consistent with the mean northward currents that *Palma et al.* [2008] find in their model over the outer half of the shelf in summer, opposing the southward summer winds. Unpublished fields from the model of M14 also show vertically integrated currents (total currents, not geostrophic) that continue along the outer shelf as far north as 33°S in December and 34° in January. This flow is consistent with the presence of the STSF in this region during summer (under a thin surface mixed layer) [*Piola et al.*, 2008a]. *Palma et al.* [2008] explain this northward flow in the face of southward winds as a result of cross-shelf pressure gradients that are established farther south by the MC. The influence of these pressure gradients spreads northward as far as 33°S due to the mechanism described by *Csanady* [1978], called the arrested topographic wave. The altimeter cannot verify the dynamics, but it does provide observational evidence for the presence of this countercurrent and its latitudinal extent, in agreement with the models of *Palma et al.* [2008] and M14 and the inferences based on hydrographic observations [*Piola et al.*, 2000, 2008a].

Observations and inferences for cross-shelf flow are much scarcer than for alongshore flow. During the winter survey in August 2003, *Piola et al.* [2008a] find filaments of fresher water extending offshore from the shelf north of the RdIP. The trajectories of water parcels with low salinity that move from the shelf to the deep ocean in the model of M14 north of the RdIP, do so in winter, tracing their origin back to the RdIP. Their preferred locations to leave the shelf have some similarity to the locations of the filaments shown by *Piola et al.* [2008a]. The trajectories of low-salinity water parcels that leave the shelf directly offshore of the RdIP are also traced back to the RdIP in the model of M14, coming directly eastward from the estuary in summer. These model calculations are consistent with the seasonal offshore flow anomalies found by the altimeter (Figures 9 and 10). North of the RdIP, between 33° and 35°S, cross-shelf velocity anomalies become eastward during winter and continue through spring, reversing in summer. North of 33°S this pattern is delayed by 2–3 months. Farther south, directly to the east and southeast of the RdIP estuary (35°–38°S), the offshore flow is strongest in summer and weakest or reversed in winter. This offshore flow is in agreement with the flow inferred by G14, who use Aquarius satellite salinity measurements to demonstrate the direct communication between the fresh water on the shelf near the RdIP estuary and the flow around eddies in the BMC in spring and summer.

As a further comparison between the model and the altimeter fields, we have used the demeaned altimeter SLA as the predictor and the model salinity fields as the predictand in a PEP calculation (Figure 11). We use the model salinity fields rather than the satellite-derived fields because the satellite data are only available after 2009, are too coarse (∼100 km cells) and are unreliable in a ∼ 100 km wide band next to the coast. The removal of the spatial mean of SLA over the shelf from each field leaves only the dynamical spatial gradients. In the first PEP mode, a band of SLA gradients and associated geostrophic currents stretch northward over the shelf from the mouth of the RdIP past 27°S. The predicted SSS pattern places fresher water
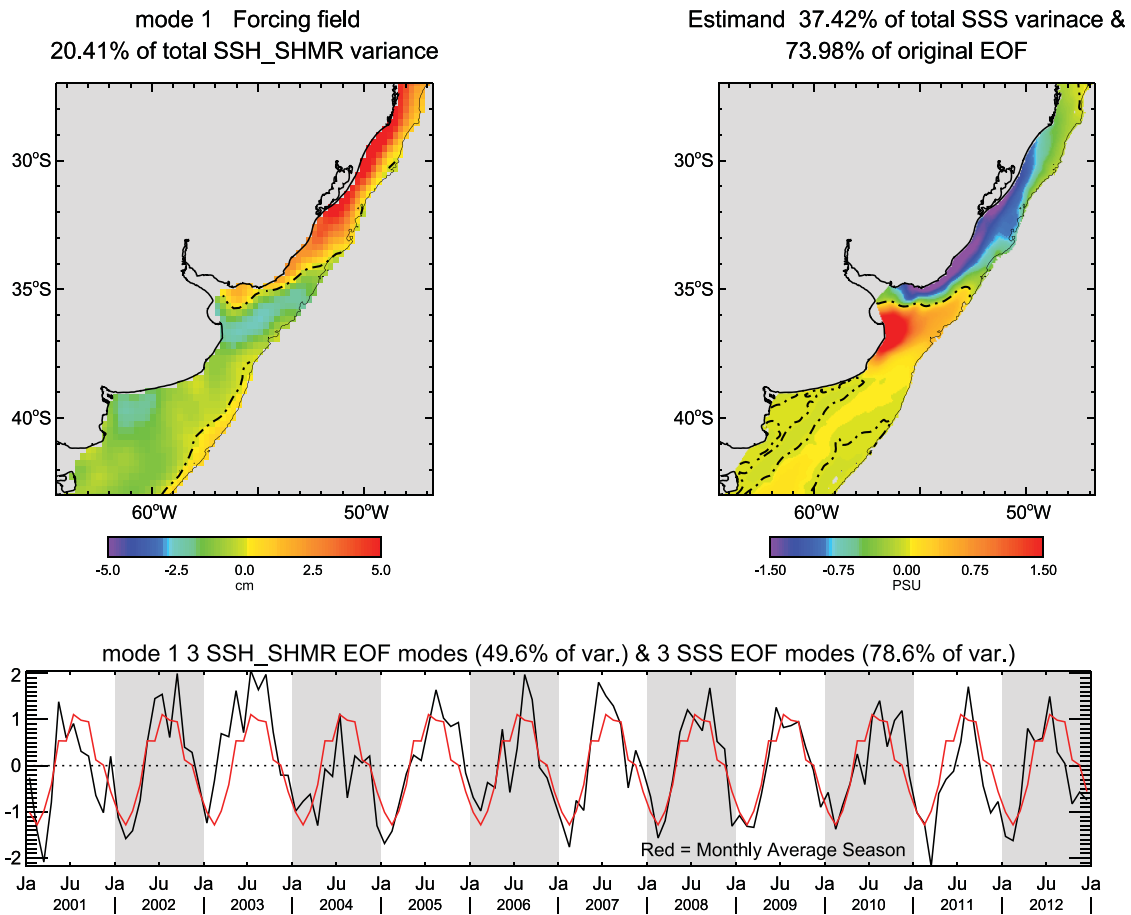
Figure 11. First PEP pattern of SLA (spatial mean removed) predicting the dominant mode of SSS from the M14 model. The spatial pattern of SLA (top left, 20.4% of the SLA variance) represents northward flow from the mouth of the RdlP and the spatial pattern of predicted SSS depicts fresher waters along the inner half of the shelf north of the RdlP (top right, 37.4% of the SSS variance). The temporal pattern (bottom) is maximum in winter and reversed in summer, at which time southward currents bring saltier water to the region north of the RdlP and trap fresher water along the southern part of the outer RdlP estuary. The 200 m isobath is shown.

next to the coast inshore of the SLA gradient, again stretching northward from the RdlP over the shelf. This mode represents 20% of the SLA variability and 37% of the salinity variability. Since the model salinity distributions are strongly controlled by the model transports, the agreement between model salinity and the altimeter's SLA gradients is primarily a demonstration that the altimeter-derived geostrophic currents are in agreement with the model transports (geostrophic and ageostrophic) over this wide shelf.

4.3. Wind Forcing Versus Steric Forcing of the SLA

The timing of the rise of SLA on the shelf as depicted by both the mean SLA over the shelf and the first EOF of raw SLA over the shelf (Figure 6) creates a maximum of height during March–April, at the end of the heating season. This suggests a contribution of seasonal heating in raising sea level over the coast (Mechanism 1). Changes in circulation can also increase sea level over the coast by transporting more mass onto the shelf. This could be caused by onshore Ekman transport due to downwelling favorable winds (Mechanism 2) or by a convergence of the large-scale currents at the boundaries of the region of interest (Mechanism 3). There is evidence for all three mechanisms in the case of the broad SW Atlantic shelf.

Regarding regional heating and steric expansion of the water column, the surface heat flux fields used to drive the model of M14 are derived in part by fields from merchant ship climatologies (COADS) and in part by internal fields and algorithms within the ROMS model. These show a long-term mean annual maximum heating (positive into the ocean) of 60–80 W m^{-2} next to the coast near 39°S. Their seasonal maximum is during November–January with values over 150 W m^{-2} south of 36°S next to the coast, remaining slightly

positive in the same southern region through March and April before becoming everywhere negative in May. Positive values return in August. The southern location of maximum heating is consistent with the timing and spatial pattern of the first EOF of raw SLA, which is maximum along the southern coast at the end of the heating season. This depiction of the heat flux isslightly different than the mean annual heating fields from two different sources presented by L. A. Ruiz-Etcheverry et al. (manuscript in preparation, 2015), who place the maximum in surface heating farther offshore, over the cold Malvinas Current next to the shelf break. When that analysis is extended to calculate the rise in sea level which would be caused by local surface heating, maximum amplitudes of 3–4 cm are found next to the coast between 40° and 48°S. Given the continued downwelling favorable alongshore winds south of 42°S (Figure 2) and the continued northward flow over the shelf during summer everywhere south of the RdlP (Figure 5), the increase in heat content in the surface layer will be concentrated toward the coast and strongest in the south, similar to the first EOF of the raw SLA in Figure 6. We also note that the SLA spatial pattern in Figure 6 is similar to that of the annual amplitude of the seasonal harmonic of SST presented by *Rivas* [2010], which reaches its annual maximum in January–February. The heating of the water column occurs in the same region and at the same time as needed to produce a steric rise in SLA, as seen in the raw SLA EOF pattern in Figure 6.

Another piece of evidence that this EOF mode is not entirely wind-driven in its southern region is the wind-forced PEP between alongshore wind stress and raw SLA (Figure 8, bottom right), which is not concentrated in the south. Its spatial maximum is nearly identical to that of the demeaned SLA, in the central and northern regions (Figure 8, bottom middle). Thus, surface heating produces a pattern consistent with the raw SLA EOF in Figure 6, while wind forcing produces the different pattern for raw SLA in Figure 8.

However, the same spatial pattern of the first PEP of wind-driven raw SLA (Figure 8, bottom right) does differ from that of the demeaned SLA, in that its spatial pattern is entirely positive. As the time series alternates between values of 1.0 in winter and −1.0 in summer, this pattern increases and decreases the mean sea level (and so the mass) over the shelf next to the coast in the middle and northern parts of our domain. Multiplying the spatial pattern by the time series produces values in winter of approximately 2.5 cm south of the RdlP and 5 cm or more north of the RdlP. We take this as evidence of a wind-driven increase in mass over the shelf, concentrated in the central and northern region of our domain and reaching a seasonal maximum in winter, minimum in summer. The timing implies a role for wind-driven Ekman transports onto the shelf.

Finally, the geostrophic currents through the northern and southern boundaries of the region change seasonally, with greater changes in the north, creating convergences over the shelf. These are balanced by outflow through the eastern boundary and by a slight change in mass over the shelf, too slight to quantify using the altimeter-derived geostrophic currents. The model results of M14 confirm and quantify this in a box model centered on the RdlP (34°–38°S), with maximum inflow from the north of ∼ 0.4 Sv in January and outflow of up to 0.2 Sv in April–July. The model transports through the southern boundary are greater but decrease to a minimum of 1.0–1.1 Sv in August–March and rise to a maximum of 1.3–1.4 Sv in April–July. Thus, although more of the inflow enters from the south, the seasonal variability is greater in the flow through the northern boundary. The flow out of the eastern boundary is approximately in balance, greatest (1.4 Sv) in November–January and least (1.0 Sv) in May–June. The north-south convergence is greatest in spring-summer and should contribute to increased sea level over the shelf before mass is forced out of the eastern boundary at the shelf break.

The model of M14 provides further evidence that the mass and volume of water over the shelf does increase seasonally. The first EOF of the model height explains 77% of the variance and is all of one sign between 27° and 43S°. It is higher next to the coast and maximum in the central region around the RdlP. Values over the coast reach a maximum of 1–2 cm between January and May. Since the model cannot increase SSH with an increase in heat content (a Boussinesq model has no steric effect), this increase in height must be a result of an increase in mass over the shelf, which could be due to both Ekman transports and the increased north-south convergences.

The analysis of altimeter data by *Saraceno et al.* [2014] also discusses the question of steric changes in height in contrast to dynamic changes. They examine altimeter data over the shelf between 27° and 40°S and find a seasonal cycle of SLA at each AVISO grid point using a 2 harmonic reconstruction. Their EOF analysis of the reconstructed SLA field finds two modes that explain all of the variance (98%), consistent with the

reconstruction from two orthogonal temporal functions. The first mode is identified as due to a steric increase in the SLA, with a maximum of 1.0–1.5 cm in all regions except those over the inner and midshelf north of the RdlP. Our January height field in Figure 3 is similar to their first mode's spatial function, where our low values north of the RdlP (purple-blue) would have near zero values in the first mode of Saraceno et al. and the rest of the field (greens and orange) would have values of 1.0, multiplied by a time function that peaks at 1.5 cm in March. Their conclusion that this is mostly a steric mode is consistent with our conclusion that the first mode of the raw SLA is strongly affected by the steric rise in the south, coupled with advection of the less dense water and also an increase of mass over the shelf. Saraceno et al. present the second EOF of the annual signal as the dynamic, wind-driven field. The spatial pattern of their second mode is the reverse of the first, with values of near 1.0 along the inner and midshelf north of the RdlP, low values elsewhere. The time series peaks in June, providing the independence of the two functions. Equatorward alongshore wind forcing explains the high coastal sea levels north of the RdlP in April–August and low SLA in September–February. Although the first EOF is identified as steric in nature, both contribute gradients in SLA that produce geostrophic currents. Using their two-harmonic reconstruction, they present monthly mean SLA fields in their Figure 11. Although there are slight differences, their SLA patterns resemble those in our Figure 3 and the supporting information. There is a slightly more pronounced pattern of south to north seasonal progression in their reconstruction, dominated by the phase relationships of their annual harmonic.

5. Conclusions

5.1. Overall

1. We find no evidence that errors in the tide models contaminate our results over the wide shelf next to South America between ~27° and 43°S (Appendix A, Figures A1–A3). Some caution should still be used in interpreting the results south of ~39°–40°S next to the coast.

2. The gridded SLA data from AVISO during the 12 year period between 2001 and 2012 allows us to examine the seasonal changes in the alongshore and cross-shelf circulation.

3. The altimeter's SLA fields do not include the mean circulation, but the AVISO mean dynamic topography (MDT) constructed from a combination of altimeter, gravity and in situ measurements compares well with the mean height of the realistic numerical circulation of M14. This gives us confidence in the realism of the model mean height field (Figure 4) and we add the model mean height to the altimeter monthly mean SLA (Figure 3) to produce a climatological seasonal cycle of monthly means of the absolute dynamic topography and geostrophic surface velocity. Altimeter and model fields (absolute surface geostrophic velocities for both, not the model's surface velocities) for January, April, July, and October are presented in Figure 5, with all months shown in supporting information.

4. EOF and PEP analysis of ECMWF wind stress and altimeter SLA fields demonstrate that a large part of the shelf seasonal SLA variability can be ascribed to wind forcing.

5. Part of the seasonal rise and fall of the SLA over the shelf is due to seasonal heating, with a stronger effect south of the RdlP, reflected in the first mode of variability of the raw SLA (Figure 6, middle).

6. Our results agree with previous analyses of hydrographic data, drifter deployments and realistic models of the circulation.

5.2. Alongshore Currents

1. South of the RdlP, mean flow is to the north all year, with weak seasonal variability (Figure 5). A slight wind-driven increase occurs in autumn-winter (April–July), most noticeable in April (Figure 3). Seasonal poleward anomalies weaken the equatorward currents in late winter and spring (August and September, supporting information) in this southern region.

2. North of the RdlP, mean currents are poleward (to the south) between 27° and 30°S, converging with equatorward currents (continuous with those south of the RdlP) offshore of the PML near 32°S. Seasonal wind-driven anomalies in the currents push the equatorward currents and convergence zone over the shelf to the north in autumn, beyond 27S° in June; poleward winds in spring reverse the current anomalies in the north, expanding the region with poleward currents southward and forcing the convergence southward to 34°–35°S (nearly to the RdlP) in December–January (Figure 5 and supporting information).

3. The transition to equatorward winds and currents is more abrupt in autumn, with sharp reversals between March and April. The switch to poleward winds and currents is more gradual in spring during August and September (Figures 6–8).

5.3. Cross-Shelf Currents

1. South of 38°S, the anomalies in the cross-shelf geostrophic currents are weak and lacking in pattern. North of 38°S, the seasonal variability of the mean cross-shelf velocities is weaker (several cm s^{-1}) in comparison to alongshore currents (several tens of cm s^{-1}), but the altimeter-derived fields demonstrate a relatively coherent evolution of their seasonal structure. Moving from south to north:

2. Between 35° and 38°S, offshore and southeast of the RdIP outflow, current anomalies are offshore during January–June and onshore during July–December.

3. Just north of the RdIP, between 34° and 35°S, the seasonal cycle is opposite to that between 35° and 38°S. Offshore velocity anomalies in winter and spring start in June and end in December. Onshore flow anomalies occur between January and May.

4. Between 27° and 32.5°S, offshore of the PML and farther north, the cross-shelf flow has a temporal pattern similar to 33°–35°S, but delayed by 2–3 months. The currents are offshore during August–March and onshore from April to July.

## Appendix A: Tidal Contamination Over the Shelf

Along the reference tracks (numbered in Figure A1, bottom right), final, corrected SLA heights (Figure A1, top) extend across the wide shelf to very close to the coast, with the editing procedures described above (section 2.1.1). Within several tens of kilometers of land, the concerns about altimeter data use are similar to those in other coastal regions: the microwave radiometer used to estimate integrated water vapor could be contaminated by land in the footprint, the wave state in shallower regions may not result in the same corrections as in the deep ocean, and (very close to land) the radar returns include reflections from land. Farther from land, the main concern is that large tidal amplitudes may not be accurately modeled and removed, leaving residual tidal errors that contaminate the analyzed fields. The periodic high-frequency nature of these tidal errors combine with lower-frequency periodic altimeter sampling to cause aliasing of the time series—creating the appearance of artificial lower-frequency signals in the sampled time series. This concern for tidal errors is greatest where the tides are large, over the shelf south of approximately 40°S [*Palma et al.*, 2004b, 2008], although aliasing can produce significant errors from moderate signals.

The altimeter signal consists of the height of the marine geoid above a reference ellipsoid (H$_G$), the "dynamical height" (H$_D$) of the ocean above or below the marine geoid (not including the tides), the height of the sum of all tidal components (the total tide signal, TT), and a number of apparent or real height signals due to electronic characteristics within the radar sensor, the atmospheric path delay of the electromagnetic signal between the satellite and the ocean surface, and environmental effects of the ocean surface (waves, etc.) [*Chelton et al.*, 2001]. We refer to the height of the sum of these other (nontidal) apparent or real signals as the total height corrections, THC. Standard altimeter data processing removes the geoid by subtracting a long temporal mean (the years 1993–2012 in standard AVISO (2014) data; or as determined by the user, in our case, 2001–2012). This removes both the stationary geoid and the mean dynamic topography (MDT, the temporal mean of the H$_D$) during that period. The remaining sea surface height anomaly, SSH$_A$ includes the "dynamical" sea level anomaly (SLA$_D$) that we want, along with the instantaneous total tides and the total height correction. We produce an estimate of the SLA$_D$ by subtracting an estimate of the total tide signals (obtained from tidal models, TT$_M$) and the sum of the other corrections, estimated from "models" of those corrections, THC$_M$.

Our estimate (SLA) of the actual dynamical sea level anomaly (SLA$_D$) is then:

$$SLA = SSH_A - TT_M - THC_M = (SLA_D + TT + THC) - TT_M - THC_M \qquad (A1)$$

If the tides and corrections are perfectly modeled, then SLA = SLA$_D$. If there are relatively small or random errors in the modeled tides and corrections, they will be reduced by averages over many realizations.
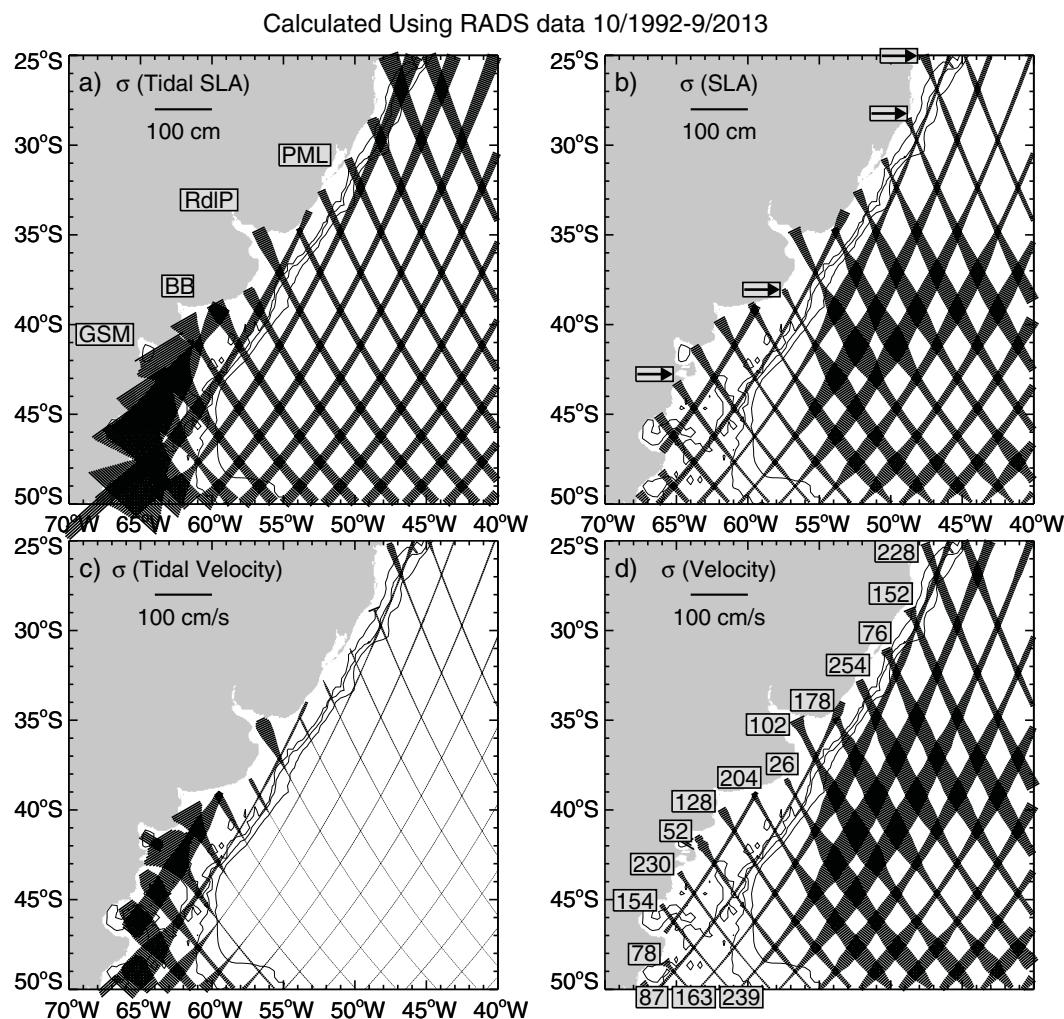
Figure A1. Standard deviations (represented by cross-bars) of the SLA heights along the altimeter tracks (a, b) and the geostrophic cross-track velocities calculated from the gradients of those heights (c, d); for the total tidal correction applied to the RADS data (a, c) and for the final corrected SLA data (b, d). Note that the analyses use 21 years of data along these reference tracks. Abbreviations for place names discussed in the text are presented in Figure A1a for the PML: Patos-Miros Lagoon; RdlP: Rio de la Plata River; BB: Bahia Blanca estuary and El Rincon Bight; GSM: Gulf of San Matias. The locations of tide gauges used for comparisons to the altimeter data are shown by arrows in Figure A1b. Track (Pass) numbers for the T/P-Jason altimeters are shown in Figure A1d. The three contours denote the 100, 200, and 1000 m isobaths.

Analysis of the time series of SLA may still alias the errors into frequencies of interest, although combinations of multiple altimeters with different sampling patterns (as in the AVISO gridded fields) should help to reduce this aliasing. However, regions with systematic errors and/or very large tides and corrections remain a concern. Over the wide Patagonian shelf, especially south of 40°S, the very large tides require that we consider the effects of errors in the modeled tidal corrections.

Saraceno et al. [2010] find relatively good agreement between the tide models and the tidal constituents estimated from tide gauges along the Patagonia coast. Given these results, we use the total tidal fields (TT$_M$) use to correct the RADS altimeter data (section 2.1.1) as an estimate of the magnitudes and spatial distribution of the real total tidal amplitudes (TT). In Figure A1a, standard deviations of the total tidal corrections at each grid point along each track are shown by the length of the crossbars along the tracks. Extreme tides occur over the shelf south of 40°S, with values next to the coast of over a meter. Moving from ∼ 40° to 39°S next to coast on tracks 128 and 204 (south and north of Bahia Blanca (BB), respectively), maximum standard deviations of tidal corrections drop from ∼50 to 30 cm. North of that, the maximum values are ∼ 20 cm or less, with the largest values in the mouth of the RdlP and next to
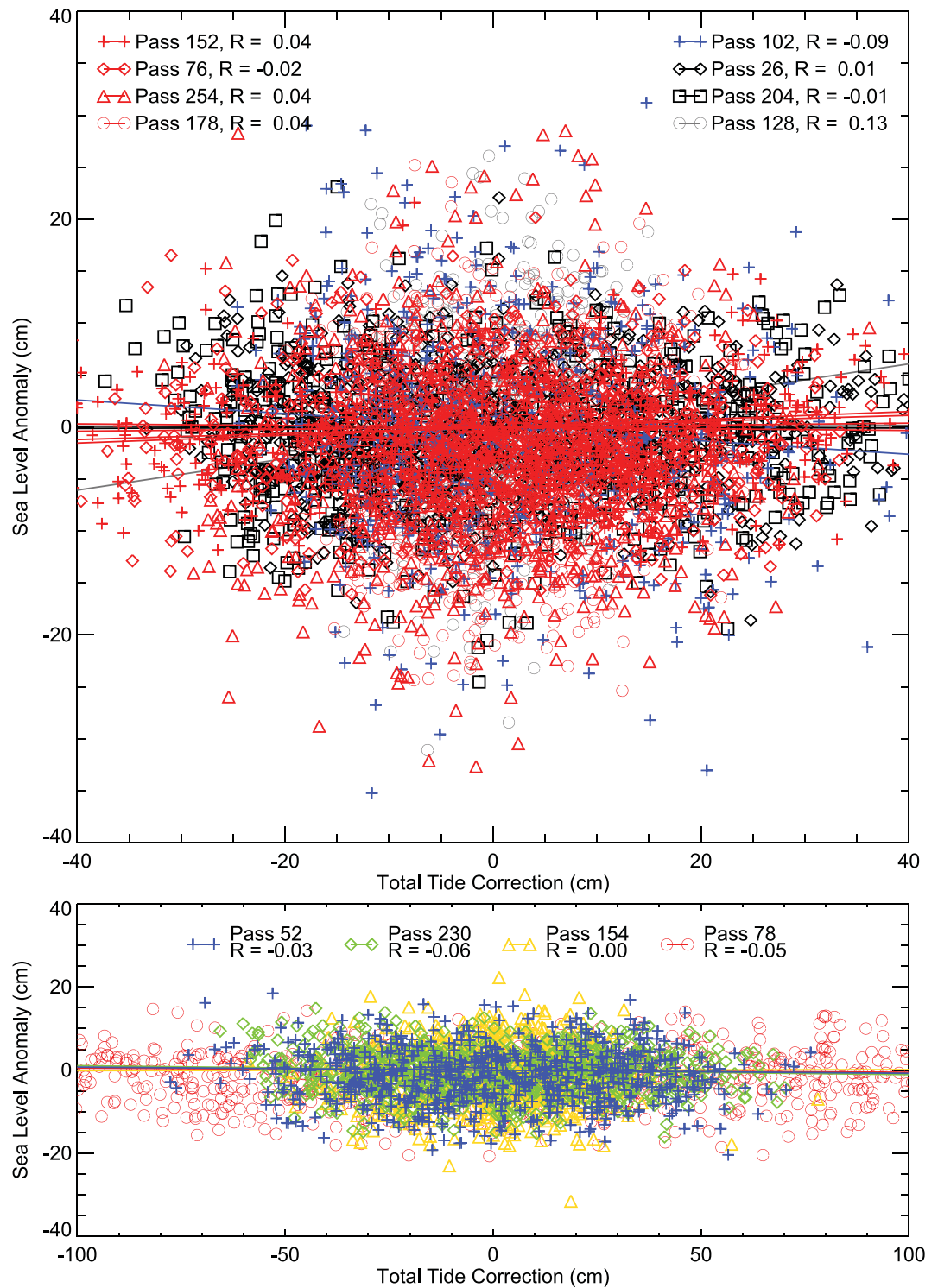
Figure A2. Scatterplots of the final corrected along-track SLA values versus the full tidal correction over the shelf. Different tracks are represented by different symbols and the correlation coefficients along each track are shown above the scatterplot. Horizontal lines represent regressions of SLA against tidal corrections. (top) Tracks north (south) of the RdP are depicted by red (black) symbols (blue for Track 102 at the mouth of the RdlP). (bottom) The four tracks south of 40° have the largest tidal heights, as represented by the 1 m range of the tidal corrections.

the coast north of 30°S. Offshore of the shelf, values are of order 10–15 cm, larger north of 35°S. These same tidal model heights are subtracted from the raw along track heights to remove the real tidal signals and form the final corrected along-track SLA signals (equation A1), shown Figure A1b. If the models
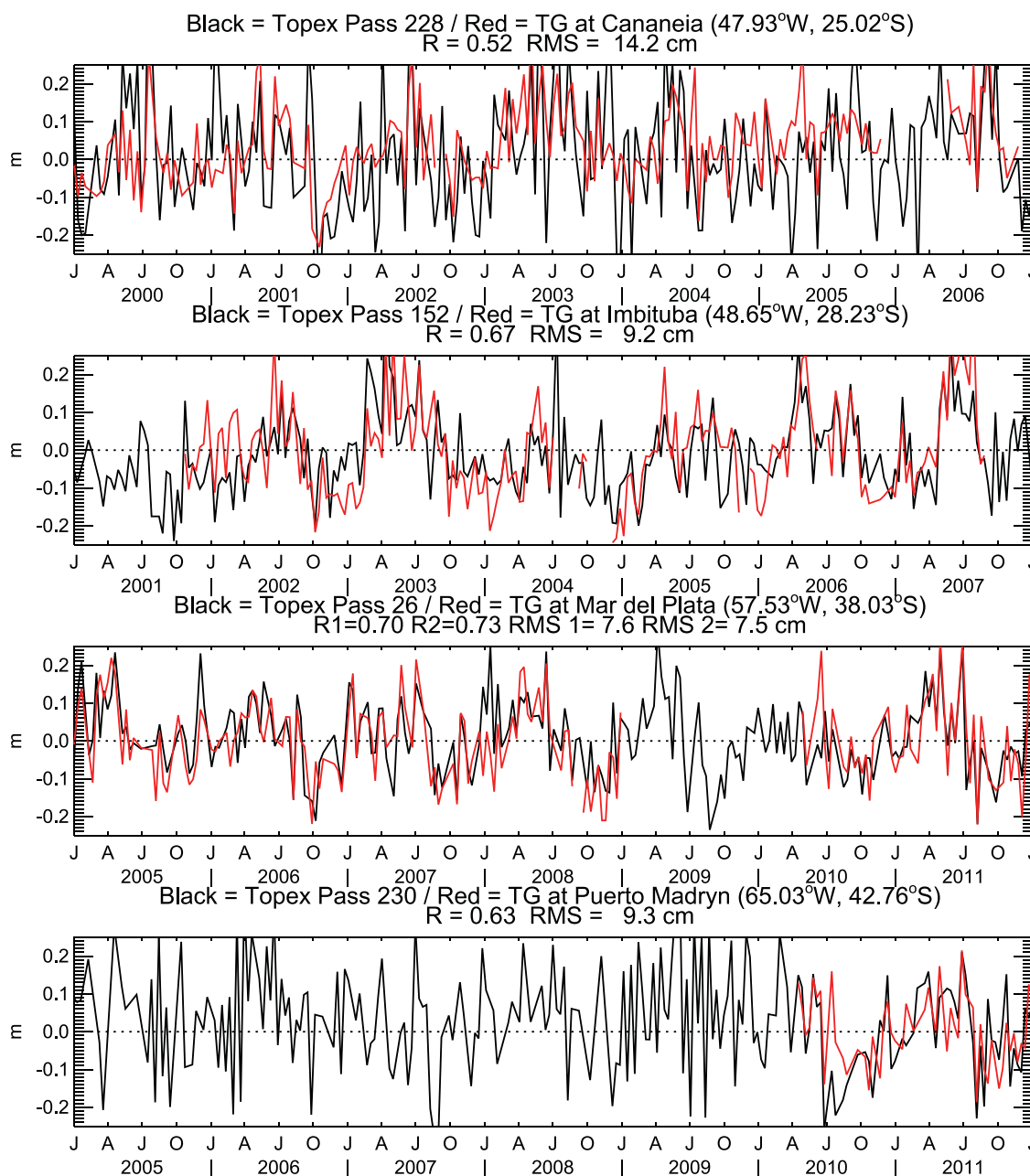
Figure A3. Comparisons of tide gauge data (red) to the nearest along-track altimeter data (black). The mean from the period of the tide gauge data has been subtracted from each time series. Correlation coefficients and RMS differences for the altimeter and tide gauge pairs are shown above each plot.

are in error, there should be a significant component of the model fields and actual tides left in the corrected SLA data. The relatively small standard deviations of the along-track SLA signals shown in Figure A1b over the shelf where the model standard deviations are large do not indicate a large amount of contamination of the signals over the shelf. There is a moderate increase in values moving from the shelf break (values ∼10 cm or less) to the coast (values ∼20 cm), giving some cause for caution in the interpretation of the SLA signals next to the coast. This is also the region where other issues with the data become important and where AVISO processing may extrapolate to the coast, giving further reasons for caution. At the same time, there are real sea level signals due to processes such as coastal trapped waves and nearshore jets that may increase SLA variance next to the coast. Also shown in Figure A1b are much larger values offshore of the shelf, which are the signatures of the energetic eddies and

meanders in the BMC, and a region of decreased SLA variance associated with the Zapiola Eddy, centered near 45°S, 45°W [*Chelton et al.*, 2011; *Saraceno and Provost*, 2012].

When the along track heights are used to calculate cross-track geostrophic velocities, the standard deviations of the velocities calculated from the tidal corrections (Figure A1c) again demonstrate larger values over the shelf south of 40°S (30–100 cm s^{-1}) and in the outer RdlP (20 cm s^{-1}). Elsewhere the velocity standard deviations created by the tidal signals are very minor, whereas the values created by the corrected along-track SLA (Figure A1d) are larger in the BMC (20–40 cm s^{-1}) and, to a lesser extent, over the shelf. We interpret the velocity variances from the corrected SLA as real signals, except where the signals from the tidal corrections are large. This is a first indication that the altimeter-derived geostrophic velocities over the shelf north of 40°S are not critically contaminated by errors in the tidal corrections.

A more quantitative test of the relation between the tidal corrections and the final SLA consists of possible correlations between the two quantities (SLA and TT$_M$) for individual observations. If the model tides are greatly different from the actual tides, there will be a component of the model tidal corrections left in the SLA signal (equation (A1)). If this is a significant fraction of the dynamic height signal, there should be a correlation between SLA and the model tidal correction. Figure A2 presents scatterplots of the data points: SLA versus total tidal corrections (TT$_M$) for each data point along the tracks over the shelf. Each track is represented by a different symbol. The horizontal lines represent linear regressions between the SLA and the tidal corrections. Figure A2 (bottom) presents the same relationships for the four tracks south of 40°S. Correlation coefficients between SLA and tidal corrections are given for each track. That most of the symbols and lines are indistinguishable from each other reflects the fact that none of the correlations or regressions are statistically significant. The largest correlation coefficients occur for the tracks that cross the coast in the bays of Bahia Blanca (Pass 128, R=0.13) and near the mouth of the RdlP (Pass 102, R= −0.09), where the largest tidal signals north of 40°S are found [*Palma et al.*, 2004b]. Similar scatterplots, correlations, and regressions (not shown) for geostrophic cross-track velocities calculated from the along-track SLA versus from the tidal corrections (as in Figures A1c and A1d) show even less correlation than for the SLA signals.

Finally, in Figure A3 we compare the 10 day SLA signals from along-track altimeter data closest to data from four coastal tide gauges (arrows in Figure A1b) at approximately 25°S (Cananeia), 28.2°S (Imbituba), 38.0°S (Mar del Plata), and 42.8°S (Puerto Madryn). At the Mar del Plata site, there are two separate time series and we treat them separately (shown overlain on the same altimeter time series in Figure A3). The tide gauge data were subsampled at the times of the nearby altimeter tracks. The correlation coefficients and RMS differences in heights are given at the top of each time series plot. These range from correlations (and RMS values) of 0.52 (14.1 cm) at 25.0°S to 0.70–0.73 (7.5–7.6 cm) at 38.0°S (the longest record). We present the time series at 42.8°S, although it is less than two years in length, to demonstrate that the comparison is not greatly degraded (r=0.64, RMS=9.0 cm), even though tidal heights increase in this region of the shelf. Since we do not expect the SLA signal at the coastal TG stations to be the same as at locations along the tracks 10–20 km offshore, this relatively good comparison gives us further confidence that the altimeter data represent the detided oceanographic signal over the shelf, even relatively close to the coast.

Based on the above results, we proceed with analyses of both SLA and geostrophic velocity anomalies over the shelf between approximately 27°–43°S, remaining cautious in our interpretation of the results south of 40°S. To do this, we use the gridded AVISO SLA data, which incorporates multiple altimeters (2–4) during our period of interest. This period (January 2001 through December 2012) is chosen partly because there are 3–4 altimeters with exact repeat tracks in operation for approximately 80% of the time. The combination of multiple altimeters used in the gridded data is needed to better resolve the shorter scales of the velocity fields over the shelf. We also choose this period to allow comparison to the results of model simulations of the circulation reported by M14. The analysis of the along-track data described above gives us confidence that the tidal corrections do not contaminate the final height and velocity signals. Random noise in the data from multiple sources is further reduced by averaging over the twelve years of data and by using methods such as EOF calculations and harmonic reconstructions, which separate the most coherent signals with seasonal variability from higher frequency noise.

References

Campos, E. J., D. Velhote, and I. C. da Silveira (2000), Shelf break upwelling driven by Brazil Current cyclonic meanders, *Geophys. Res. Lett.* *27*(6), 751–754.

Campos, P., O. O. Möller, A. R. Piola, and E. D. Palma (2013), Seasonal variability and western boundary upwelling: Cape Santa Marta (Brazil), *J. Geophys. Res. Oceans*, *118*, 1420–1433, doi:10.1002/jgrc.20131.

Castro, B. M., and L. B. Miranda (1998), Physical oceanography of the western Atlantic continental shelf located between 4°N and 34°S, in *The Sea: Coastal Oceanography*, vol. 11, edited by A. R. Robinson and K. H. Brink, pp. 209–251, John Wiley, N. Y.

Chelton, D. B., J. C. Ries, B. J. Haines, L. L. Fu, and P. S. Callahan (2001), Satellite Altimetry, in *Satellite Altimetry and Earth Sciences*, edited by L.-L. Fu and A. Cazenave, pp. 1–131, chap. 1, Academic Press, San Diego, Calif.

Chelton, D. B., M. G. Schlax, and R. M. Samelson (2011), Global observations of nonlinear mesoscale eddies, *Prog. Oceanogr. 91*, 167–216, doi:10.1016/j.pocean.2011.01.002.

Combes, V., and R. P. Matano (2014), A two-way nested simulation of the oceanic circulation in the Southwestern Atlantic, *J. Geophys. Res. Oceans*, *119*, 731–756, doi:10.1002/2013JC009498.

Csanady, G. T. (1978), The arrested topographic wave, *J. Phys. Oceaongr.*, *8*, 47–62.

Davis, R. E. (1977), Techniques for statistical analysis and prediction of geophysical fluid systems, *Geophys. Astrophys. Fluid Dyn.*, *8*, 245–277.

Davis, R. E. (1978), Predictability of sea level pressure anomalies over the North Pacific Ocean, *J. Phys. Oceanogr.*, *8*, 233–246.

Framiñan, M. B., A. Valle-Levinson, H. H. Sepúlveda and O. B. Brown (2008), Tidal variations of flow convergence, shear, and stratification at the Rio de la Plata estuary turbidity front., *J. Geophys. Res.*, *113*, C08035, doi:10.1029/2006JC004038.

Ghisolfi, R. D. and W. D. McKee (2003), The effects of the alongshore wind stress on the top-to-bottom front along the Southern Brazilian coast: A two-dimensional modelling approach, *Cont. Shelf Res.*, *23*, 1401–1424.

Gordon, A. L. (1989), Brazil-Malvinas Confluence−1984, *Deep Sea Res., Part A, 36*, 359–384.

Gordon, A. L., and C. L. Greengrove (1986), Geostrophic circulation of the Brazil-Falkland Confluence, *Deep Sea Res., Part A, 33*, 573–585, doi:10.1016/0198-0149(86)90054-3.

Goni, G. J., and I. Wainer (2001), Investigation of the Brazil Current front variability from altimeter data, *J. Geophys. Res.*, *106*(C12), 13,117–31,128.

Guerrero, R. A., A. R. Piola, H. Fenco, R. P. Matano, V. Combes, Y. Chao, C. James, E. D. Palma, M. Saraceno, and P. T. Strub (2014), The salinity signature of the cross-shelf exchanges in the Southwestern Atlantic Ocean: Satellite Observations, *J. Geophys. Res. Oceans*, *119*, 7794–7810, doi:10.1002/2014JC010113..

Liu, Y., R. H. Weisberg, S. Vignudelli, L. Roblou, and C. l. R. Merz (2012), Comparison of the X-TRACK altimetry estimated currents with moored ADCP and HF radar observations on the West Florida Shelf, *Adv. Space Res.*, *50*(8), 1085–1098.

Lucas, A. J., R. A. Guerrero, H. W. Mianzán, M. E. Acha, and C. A. Lasta (2005), Coastal oceanographic regimes of the Northern Argentine continental shelf (34–43°S), *Estuarine Coastal Shelf Sci.*, *65*, 405–420, doi:10.1016/j.ecss.2005.06.015.

Matano, R. P., M. G. Schlax, and D. B. Chelton (1993), Seasonal variability in the southwestern Atlantic, *J. Geophys. Res.*, *98*(C10), 18,027–28,035.

Matano, R. P., E. D. Palma, and A. R. Piola (2010), The influence of the Brazil and Malvinas Currents on the southwestern Atlantic shelf circulation, *Ocean Sci.*, *6*(4), 938–995.

Matano, R. P., V. Combes, A. R. Piola, R. Guerrero, E. D. Palma, P. T. Strub, C. James, H. Fenco, Y. Chao, and M. Saraceno (2014), The salinity signature of the cross-shelf exchanges in the Southwestern Atlantic Ocean: Numerical simulations, *J. Geophys. Res. Oceans*, *119*, 7949–7968, doi:10.1002/2014JC010116.

Möller, O. O., Jr., A. R. Piola, A. C. Freitas, and E. J. D. Campos (2008), The effects of river discharge and seasonal winds on the shelf off Southeastern South America, *Cont. Shelf Res.*, *28*, 1607–1624.

Olson, D. L., G. P. Podesta, R. H. Evans, and O. Brown, (1988), Temporal variations in the separation of Brazil and Malvinas currents, *Deep Sea Res., Part A, 35*, 1971–1990.

Palma, E. D., R. P. Matano, and A. R. Piola (2004a), A comparison of the circulation patterns over the southwestern Atlantic shelf driven by different wind climatologies, *Geophys. Res. Lett.*, *31*, L24303, doi:10.1029/2004GL021068.

Palma, E. D., R. P. Matano, and A. R. Piola (2004b), A numerical study of the southwestern Atlantic shelf circulation: Barotropic response to tidal and wind forcing, *J. Geophys. Res.*, *109*, C08014, doi:10.1029/2004JC002315.

Palma, E. D., R. P. Matano, and A. R. Piola (2008), A numerical study of the southwestern Atlantic shelf circulation: Stratified ocean response to local and offshore forcing, *J. Geophys. Res.*, *113*, C11010, doi:10.1029/2007JC004720.

Palma, E. D., and R. P. Matano (2009), Disentangling the upwelling mechanisms of the South Brazil Bight, *Cont. Shelf Res.*, *29*, 1525–1534.

Pereira, C. S. (1989), Seasonal variability in the coastal circulation on the Bazilian continental shelf (29°S − 35°S), *Cont. Shelf Res.*, *9*, 285–299, doi:10.1016/0278-4343(89)90029-0.

Piola, A. R., J. D. Campos, O. O. Moller Jr., M. Charo, and C. Martinez (2000), Subtropical shelf front off eastern South America, *J. Geophys. Res.*, *105*(C3), 6566–6578.

Piola, A. R., R. P. Matano, E. D. Palma, O. O. Möller, and E. J. D. Campos (2005), The influence of the Plata River discharge on the western South Atlantic Shelf, *Geophys. Res. Lett.*, *32*, L01603, doi:10.1029/2004GL021638.

Piola, A. R., O. O. Moller Jr., R. A. Guerrero, and E. J. D. Campos (2008a), Variability of the Subtropical Shelf front off eastern South America: Winter 2003 and summer 2004, *Cont. Shelf Res.*, *28*, 1639–1648, doi:10.1016/j.csr.2008.03.013.

Piola, A. R., S. I. Romero, and U. Zajaczkovski, (2008b), Space-time variability of the Plata plume inferred from ocean color, *Cont. Shelf Res.*, *28*, 1556–1567, doi:10.1016/j.csr.2007.02.013.

Rio, M. H., P. M. Poulain, A. Pascual, E. Mauri, G. Larnicol, and R. Santoleri (2007), A mean dynamic topography of the Mediterranean Sea computed from altimetric data, in-situ measurements and a general circulation model, *J. Mar. Syst.*, *65*(14), 484–508.

Risien, C. M., and D. B. Chelton (2008), A global climatology of surface wind and wind stress fields from eight years of QuikSCAT scatterometer data, *J. Phys. Oceanogr.*, *38*, 2379–2413, doi:10.1175/2008JPO3881.1.

Rivas, A. L. (1997), Current-meter observations in the Argentine Continental Shelf, *Cont. Shelf Res.*, *17*(4), 391–406.

Rivas, A. L. (2010), Spatial and temporal variability of satellite-derived sea surface temperature in the southwestern Atlantic Ocean, *Cont. Shelf Res.*, *30*, 752–760.

Roblou, J., J. Lamourous, J. Bouffard, F. Lyard, M. Le Henaff, A. Lonbard, P. Marsaleix, P. De Mey, and F. Birol (2011), Post-processing altimeter data towards coastal applications and integration into coastal models, in *Coastal Altimetry*, edited by S. Vignudellie et al. pp. 217–246, Springer, Berlin, doi:10.1007/978-3-642-12796-0_9.

Ruiz Etcheverry, L. A., M. Saraceno, A. R. Piola, G. Valladeau, and O. O. Möller (2015), A comparison of the annual cycle of sea level in coastal areas from gridded satellite altimetry and tide gauges, *Cont. Shelf Res.*, *92*, 87–97.

Saraceno, M., and C. Provost (2012), On eddy polarity distribution in the Southwestern Atlantic, *Deep Sea Res., Part 1*, *69*, 62–69.

Saraceno, M., E. E. D. D'Onofrio, M. E. Fiore, and W. H. Grismeyer (2010), Tide model comparison over the Southwestern Atlantic Shelf, *Cont. Shelf Res.*, *30*(17), 1865–1875.

Saraceno, M., C. G. Simionato, and L. A. Ruiz Etcheverry (2014), Sea surface height trend and variability at seasonal and interannual time scales in the Southeastern South American continental shelf between 27°S and 40°S, *Cont. Shelf Res.*, *91*, 82–94. [Available at http://dx.doi.org/10.1016/j.csr.2014.09.002.]

Simionato, C. G., M. N. Nuñez, and M. Engel (2001), The salinity front of the Río de la Plata-A numerical case study for winter and summer conditions, *Geophys. Res. Lett.*, *28*(13), 2641–2644.

Soares, I. D., V. Kourafalou, and T. N. Lee (2007), Circulation on the western South Atlantic continental shelf. 2: Spring and autumn realistic simulation, *J. Geophys. Res.*, *112*, C04003, doi:10.1029/2006JC003620.

Strub, P. T., C. James, A. C. Thomas, and M. R. Abbott (1990), Seasonal and nonseasonal variability of satellite-derived surface pigment concentration in the California Current, *J. Geophys. Res.*, *95*(C7), 11,501–11,530.

Strub, P. T., T. K. Chereskin, P. P. Niiler, C. James, and M. D. Levine, (1997), Altimeter-derived variability of surface velocities in the California Current System; 1. Evaluation of TOPEX altimeter velocity resolution, *J. Geophys. Res.*, *102*(C6), 12,727–12,748.

Wainer, I., P. Gent, and G. Goni (2000) Annual cycle of the Brazil-Malvinas confluence region in the National Center for Atmospheric Research Climate System model. *J. Geophys. Res. 105*(C11), 26,167–26,177.

Zavialov, P. O., O. O. Möller, and E. J. D. Campos (2002), First direct measurements of currents on the continental shelf of southern Brazil, *Cont. Shelf. Res.*, *22*, 1975–1986, doi:10.1016/S0278-4343(02)00049-3.